

T-4134

EARTHQUAKE SOURCE MECHANISM
DETERMINATION FROM REGIONAL
WAVEFORMS

by

Hayrullah Karabulut

ARTHUR LAKES LIBRARY
COLORADO SCHOOL OF MINES
GOLDEN, CO 80401

ProQuest Number: 10783772

All rights reserved

INFORMATION TO ALL USERS

The quality of this reproduction is dependent upon the quality of the copy submitted.

In the unlikely event that the author did not send a complete manuscript and there are missing pages, these will be noted. Also, if material had to be removed, a note will indicate the deletion.



ProQuest 10783772

Published by ProQuest LLC (2018). Copyright of the Dissertation is held by the Author.

All rights reserved.

This work is protected against unauthorized copying under Title 17, United States Code
Microform Edition © ProQuest LLC.

ProQuest LLC.
789 East Eisenhower Parkway
P.O. Box 1346
Ann Arbor, MI 48106 – 1346

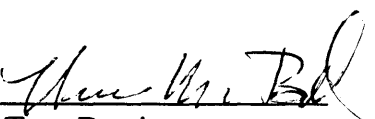
T-4134

A thesis submitted to the faculty and Board of Trustees of the Colorado School of Mines in partial fulfilment of the requirement for the degree of Master of Science, Geophysical Engineering.

Golden, Colorado

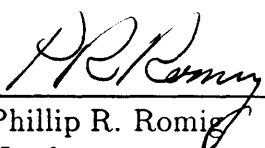
Date 6 January 1992

Signed: 
Hayrullah Karabulut

Approved: 
Tom Boyd
Thesis Advisor

Golden, Colorado

Date 13 January 1992


Phillip R. Romig
Head
Department of Geophysics

ABSTRACT

A set of computer simulations are performed to recover earthquake source parameters from regional waveforms. Lateral variations in earth structure are represented by randomly perturbing a reference earth model. The Green's functions are calculated using the Reflectivity method for three elementary source mechanisms. Seismograms are obtained by combining three elementary sources with appropriate weighting coefficients which are functions of the moment tensor components. Parameterizations are developed using the seismograms and their envelopes. These parameterizations include; area, energy, and statistical moments of waveform envelopes. The parameterizations are evaluated by performing a grid search over the pertinent source parameters; strike (ϕ_s), dip (δ) and slip (λ) of the fault plane, and seismic moment. For these initial tests the source depth is fixed.

A large number of experiments are performed to understand the nature of the solution space. Parameterizations are tested for their sensitivity to different source mechanisms and structural variations. The experiments show that energy and statistical moments can be employed for source mechanism determination. We also experiment with different time windows, (i.e., P-wave, Surface wave), for each parameterization.

The results indicate that source parameters, ϕ_s , δ and λ , can be determined to within $\pm 20^\circ$. The error in source parameters is maximum when the slip is near to 90° .

Solutions are well constrained for $10^\circ < \delta < 80^\circ$, $20^\circ < \lambda < 160^\circ$. Multiple solutions are found by performing grid search over the parameter space. The nonuniqueness' observed generally fall into two categories: 1) conjugate solutions and, 2) solutions that resolve because of the shallow depth of the assumed source.

Least squares inversion is performed on the source parameters and the solutions are compared to the results of the grid search. The inversion results show that solutions can be determined with greater accuracy if a smaller search spacing is used. The solutions found after inversion are not unique. Different solutions are obtained by using different initial guesses.

Table of Contents

List of Figures	vi
List of Tables	ix
1 INTRODUCTION	1
2 CALCULATION OF SYNTHETIC SEISMOGRAMS	7
2.1 P-wave	7
2.2 SV-wave	12
2.3 SH-wave	15
3 REFLECTIVITY METHOD	18
3.1 Introduction	18
3.2 Method	20
4 INVERSION OF THE GEOPHYSICAL DATA	26
4.1 Linear least-squares inversion	26
4.2 Singular Value Decomposition	28
5 DATA ANALYSIS	30
5.1 Introduction	30
5.2 Quantitative analysis of the seismograms	31
5.3 Parameterization of the wavefield	34
5.4 Grid Search	52
5.5 Inversion	76
6 CONCLUSIONS	82
A THE HILBERT TRANSFORM	89

List of Figures

2.1	Cartesian coordinate system used in source mechanism studies. From Aki and Richards (1980).	7
2.2	<i>P-wave</i> radiation pattern for a vertical strike slip fault.	11
2.3	<i>SV-wave</i> radiation pattern for a vertical strike slip fault.	14
2.4	<i>SH-wave</i> radiation pattern for a vertical strike slip fault.	17
3.1	Layered medium and equation parameters. The source is located at z_s under the z_m interface. Layer parameters are: $\alpha_i = P$ velocity, $\beta_i = S$ velocity, $\gamma_i =$ density, $d_i =$ thickness, z_i depth to the top. From Kind (1985).	21
5.1	Reference Earth model used in the calculation of the fundamental Green's functions. Observed seismograms are calculated using earth models which are random perturbations of the reference models. From Kind(1985).	33
5.2	Three vertical component fundamental Green's functions. Vertical dip slip is shown on top, vertical strike slip in the middle and 45° dip slip on the bottom.	35
5.3	Two tangential component fundamental Green's functions. Vertical dip slip is shown on top, 45° dip slip on the bottom.	36
5.4	Vertical component seismograms for the three fundamental source types calculated for a model with velocities lower than the reference model.	37
5.5	Vertical component seismograms for the three fundamental source types calculated for a model with velocities higher than the reference model.	38
5.6	Selected observed (first row) and calculated seismograms (second row) for the <i>P-wave</i> time window and the correlation between the area of the observed and calculated seismograms. The correlation coefficient is 0.9.	41

5.7	Selected observed (first row) and calculated seismograms (second row) for the <i>surface wave</i> time window and correlation between the area of the observed and calculated seismograms. The correlation coefficient is 0.52.	42
5.8	Selected observed (first row) and calculated seismograms (second row) for the <i>P-wave</i> time window and correlation between the energy of the observed and calculated seismograms. The correlation coefficient is 0.77.	43
5.9	Selected observed (first row) and calculated seismograms (second row) for the <i>surface wave</i> time window and correlation between the energy of the observed and calculated seismograms. The correlation coefficient is 0.97.	44
5.10	Envelopes of the 3 fundamental seismograms shown in Figure 5.2. . .	46
5.11	Observed seismogram (top), its envelope (middle), and changes in the kernel function of the moments of envelope (bottom).	47
5.12	Selected observed (first row) and calculated seismograms (second row) for the <i>P-wave</i> time window and the correlation between the moments of the envelopes of the observed and calculated seismograms. M is the total moment.	49
5.13	Selected observed (first row) and calculated seismograms (second row) for the surface time window and the correlation between the moments of the envelopes of the observed seismograms and calculated seismograms. M is the total moment.	50
5.14	Selected observed (first row) and calculated seismograms (second row) for the tangential component and the correlation between the moments of the envelopes of the observed and calculated seismograms. M is the total moment	51
5.15	RMS error surface using the first three statistical moments of the <i>P-wave</i> envelope. A source mechanism of $\phi_s = 30^\circ, \delta = 60^\circ, \lambda = 60^\circ$ is used to generate the observed seismograms. The lower right-hand portion of the figure shows the error surface from a grid search of the solution space. The circle to the left shows the azimuthal distribution of observations, and several examples of the observed and computed waveforms are generated from the best solution found in the grid search. Plot saturation occurs at misfits of 0.07 and 0.22. The actual misfits range between 0.05 and 0.24.	55
5.16	A slice through the error surface at $\lambda = 60^\circ$ in Figure. Plot saturation occurs at misfits of 0.04 and 0.28. The actual misfits range between 0.035 and 0.30.	56

5.17 A slice through the error surface shown in Figure at $\lambda = 130^\circ$. Plot saturation occurs at misfits of 0.032 and 0.25. The actual misfits range from between 0.032 and 0.27. 57

5.18 RMS error surface using the first three statistical moments of the *Surface wave* envelope. A source mechanism of $\phi_s = 0^\circ, \delta = 90^\circ, \lambda = 0^\circ$ is used to generate the observed seismograms. The lower right-hand portion of the figure shows the error surface from a grid search of the solution space. The circle to the left shows the azimuthal distribution of observations, and several examples of the observed and computed waveforms are generated from the best solution found in the grid search. Plot saturation occurs at misfits of 0.22 and 0.35. The actual misfits range from between 0.07 and 0.44. 58

5.19 RMS error surface using the first 3 statistical moments of the tangential component. A source mechanism of $\phi_s = 30^\circ, \delta = 60^\circ, \lambda = 60^\circ$ is used to generate the observed seismograms. The lower right-hand portion of the figure shows the error surface from a grid search of the solution space. The circle to the left shows the azimuthal distribution of observations, and several examples of the observed and computed waveforms are generated from the best solution found in the grid search. Plot saturation occurs at misfits of 0.12 and 0.55. 60

5.20 A slice through the error surface at $\lambda = 60^\circ$ in Figure . Plot saturation occurs at misfits of 0.08 and 0.48. The actual misfits range from between 0.0 and 0.55. 61

5.21 P waveforms generated at 2 different azimuths (top) are identical for two different source mechanisms (bottom) found after the grid search. 73

5.22 The change in the RMS error with iteration using moments of the *P-wave* envelopes. 78

5.23 The change in the RMS error with iteration using moments of the *P-wave* envelopes. 79

5.24 The change in the RMS error with iteration using moments of the surface wave envelopes. 80

5.25 The change in the RMS error with iteration using moments of the surface wave envelopes. 81

A.1 The kernel $(-\pi t)^{\frac{1}{2}}$ and its Fourier transform *i sign s*. Bracewell(1986). 90

List of Tables

5.1	Source mechanism solutions after a grid search using the <i>P-waves</i> energy.	63
5.2	Source mechanism solutions after a grid search using the <i>Surface waves</i> energy.	65
5.3	Source mechanism solutions after a grid search using the <i>P-waves</i> envelope.	67
5.4	Source mechanism solutions after a grid search using the <i>Surface waves</i> envelope.	69
5.5	Moment tensor ($\phi_s = 0^\circ, \delta = 90^\circ, \lambda = 90^\circ$).	71
5.6	Moment tensor for two different source mechanisms ($\phi_s = 80^\circ, \delta = 50^\circ, \lambda = 130^\circ$ and $\phi_s = 30^\circ, \delta = 60^\circ, \lambda = 60^\circ$).	71
5.7	Coefficients of fundamental Green's functions	74
5.8	A summary of Tables 5.1-5.4.	75
5.9	The estimated source parameters from an initial set of parameters. . .	78
5.10	The estimated source parameters from an initial set of parameters. . .	79
5.11	The estimated source parameters from an initial set of parameters. . .	80
5.12	The estimated source parameters from an initial set of parameters. . .	81

ACKNOWLEDGEMENTS

Throughout my studies in C.S.M and the development of this thesis, I benefited greatly from the guidance and encouragement of my thesis committee: Prof. Thomas M. Boyd, Dr. Stu Sipkin, Prof. Frank Hadsell, and Prof. Ronald N. Knoshaug.

Professor Boyd and Dr. Sipkin suggested the subject and supplied many valuable insights. I am indebted to Dr. Boyd and Dr. Sipkin for their long discussions and encouragements in this effort.

I would like to express my sincere appreciation to the I.T.U., Departement of Geophysics in TURKEY.

With appreciation, I gratefully acknowledge D.F. Lane for his time and valuable discussions.

I would like to thank to my parents my friends and my wife for their love and patience.

Chapter 1

INTRODUCTION

Like exploration seismologists, earthquake seismologists are interested in determining the structure of the earth using seismic waveforms and travel times. Earthquakes, however, are not controlled sources. Not only are their locations and depths unknown, but the rate of energy release may be complicated, and the energy is not released in a spherically symmetric fashion. It can, therefore, be difficult to separate path effects, mode conversions, attenuation, and scattering from source complications.

By in large, seismic sources appear to occur because of shear-dislocations along planer-fault surfaces. The simplest force representation of such a point source is given by a double couple system, which is characterized by a seismic moment and orientation. Commonly, the orientation is specified by fault strike, dip, and the direction of slip along the fault plane. These parameters constitute the earthquake source mechanism.

The history of source mechanism studies may be traced back to the late 1920's.

Nakano (1923) was the first to show that, at large distances from the source a double couple force system results in a quadrantal distribution of the direction of *P-wave* first motion. Since that time, progresses has been made in this field by many researchers (e.g., Byerly, 1955, Hodgson, 1953, Stauder, 1962, etc.). At great distances from the source, because of ray bending and the earth's spherical geometry, the distribution of first motions is difficult to infer. Byerly (1955) proposed a graphical technique that projects a global distribution of data onto a plane through which compressional and dilatational quadrants can be constructed. Frequently, however, first motion observations are not adequate to determine the focal mechanism. A large number of observing stations must be used to get a well constrained mechanism and, given the distribution of recording stations, the available observations may not be sufficient to constrain either or both of the nodal planes. In addition to *P-wave* first motions, other properties of the wavefield have been used to constrain source parameters. Keilis-Borok (1959) developed a technique based on the sign combination of *P*, *SV*, *SH-waves*. Honda (1962) used amplitude ratio of the *P* to *S*. Another technique uses the polarization angle of *S-waves* (Nuttli and Whitmore, 1962). The polarization angle is calculated from the amplitude ratio *SH* and *SV*. Theoretical distributions of the polarization angle are calculated and compared to observations. The use of *S-waves* can resolve some of the ambiguity of the *P-wave* solution.

By using a moment tensor representation of the source (Gilbert, 1971), it is

possible to invert a given set of observations to determine the source parameters. The method is valid for free oscillations (Gilbert and Dziewonski, 1975), surface waves (McCovan, 1976) and body waves (Stump, 1976). Inverting for moment tensor, however, is not always a suitable technique for determining the most appropriate source model for a given set of observations. This is because different source models have different numbers of free parameters, and in the presence of errors, the solution favors the model with the greatest number of free parameters (Strelitz, 1978).

During the past decade, waveform modelling has become an important tool for studying faulting processes. This is partly because computers have allowed us to calculate synthetic seismograms for complex earth models and partly because of the increased availability of high quality digital data. Various techniques for the inversion of teleseismic body waves have been devised including Helmberger (1974), Langston and Helmberger (1975), Stump and Johnson (1982), Sipkin (1982), and Nábělek (1984). Langston and Helmberger (1975) developed an inversion method based on generalized ray techniques for teleseismic waves. The method may include body waves or surface waves of any type with the restriction that the structure must be plane layered and known. Stump and Johnson (1977) inverted for moment tensor using singular value decomposition. Nábělek's (1984) nonlinear inversion solves for strike, dip, slip, depth, and source time function using a form of constrained inversion. Sipkin (1982) introduced a waveform inversion technique based on moment tensor

representation of seismic sources by using multichannel signal-enhancement theory and multichannel vector deconvolution methods.

In general, the success of waveform modeling depends on the calculation of the Green's functions and an initial estimate of the source parameters. The Green's functions for teleseismically recorded waveforms can be calculated adequately because the longer wavelengths, which are recorded at these distances can be well modeled using standard, radially symmetric earth models. At regional distances, however, the earth structure must be modeled with a greater accuracy since the shorter wavelengths recorded at these distance ranges are more sensitive to variations in earth structure and the ray paths observed spend most of their time in a crust which is very heterogeneous. If the earth structure is not well known, the calculated Green's functions will not be sufficiently accurate and the source mechanism will be determined poorly.

Determining source parameters from regional data is important for several reasons. Shallow, moderate size earthquakes ($M < 6$) may not be recorded at teleseismic distances. These events have widespread geographic occurrence, and in some cases these earthquakes provide the only clues to the tectonics of a region. Their widespread occurrence also makes these events desirable sources for crustal structure studies (Wallace,1978).

In this study, we will develop a technique for determining source mechanisms from regionally recorded waveforms. To be successful, our parameterization must

be insensitive to variations in earth structure while remaining sensitive to variations in source mechanism. These parameterizations may include area, energy, statistical moments of seismograms' envelopes and may be calculated for different time windows, P , S and surface waves as well as for the entire seismogram. To test these parameterizations, computer simulations in varying earth structures are done. While a grid search is performed to understand the solution space, an inversion technique is developed to extract source characteristics from these parameterizations. Combining different components of the observed wavefield may help eliminate local minima, and P -wave polarity information can be used to eliminate some of the solutions. We will calculate the Green's functions using the well-known result that an arbitrarily oriented point source dislocation can be represented as the sum of a vertical strike-slip, vertical dip-slip, and 45° dipping dip-slip sources. The advantage of decomposing seismograms into three fundamental components is that Green's functions for an arbitrarily oriented source at any azimuth are calculated by combining them with appropriate weighting coefficients. Therefore, we only need three fundamental Green's functions for a specified earth model to obtain a set of seismograms with different source mechanisms and at different azimuths.

As mentioned earlier, everything done in this study is a computer simulation. Theoretical seismograms are calculated for a standard reference model. The reference model is perturbed and observed seismograms are calculated. We then attempt

to extract source parameters from the observed waveforms using Green's functions calculated from the reference model.

The inverse problem can be solved in one of two ways: 1) First, we can determine the weighting coefficients for the fundamentals and parameters for these coefficients, or 2) We can directly determine source parameters from the parameterization of the seismograms. The determination of weighting coefficients and source parameters may be a linear or nonlinear process depending on the parameterization. But nonlinear inversion has the advantage that nonlinear constraints can be imposed easily.

Seismograms are calculated by using the Reflectivity Method (Kennett,1983). The reflectivity method has the advantage over ray-theoretical methods (Chapmann and Orcutt, 1985) in that the complete earth response can be obtained. In order to calculate the earth response, one needs to specify only the structural model and the frequency bandwidth. Partial responses can be calculated for a chosen slowness or ray parameter window. The only disadvantage is that it is computationally expensive.

Chapter 2

CALCULATION OF SYNTHETIC SEISMOGRAMS

2.1 P-wave

Let's introduce Cartesian coordinate directions \hat{x} , \hat{y} , \hat{z} at the epicenter. Our choice is \hat{x} = North, \hat{y} =East, and \hat{z} = vertical downward, as shown in Figure 2.1.

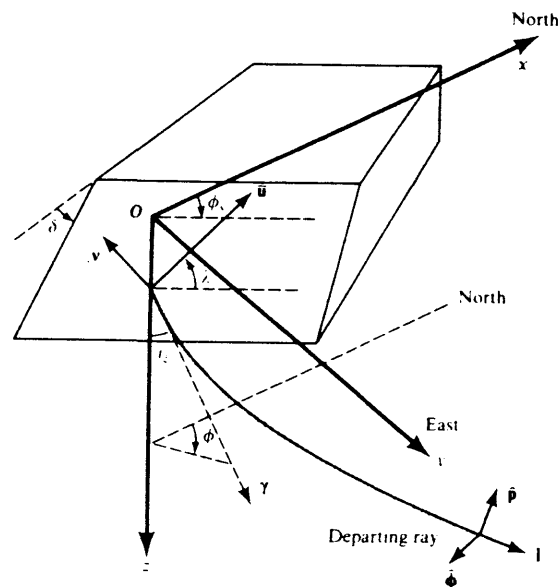


Figure 2.1: Cartesian coordinate system used in source mechanism studies. From Aki and Richards (1980).

The far-field *P-wave* displacement at position x and time t caused by an arbitrary source is given by Aki and Richard (1980) as

$$\mathbf{u}^P(\mathbf{x}, t) = \frac{F^P \mu A}{4\pi\alpha^3 r \rho} \bar{u}\left(t - \frac{r}{\alpha}\right) \hat{\mathbf{l}}. \quad (2.1)$$

Let

$$G = \frac{\mu A}{4\pi\alpha^3 r \rho},$$

then

$$\mathbf{u}^P(\mathbf{x}, t) = F^P G \bar{u}\left(t - \frac{r}{\alpha}\right) \hat{\mathbf{l}}, \quad (2.2)$$

where, A is the amplitude of the source time function, α is *P-wave* velocity, ρ is density, μ is shear modulus, r is the distance, \bar{u} is the particle velocity at the source. $\hat{\mathbf{l}}$ is the direction cosine of the observed *P-wave*, and is given by

$$\hat{\mathbf{l}} = \gamma = \sin i_\xi \cos \phi \hat{\mathbf{x}} + \sin i_\xi \sin \phi \hat{\mathbf{y}} + \cos i_\xi \hat{\mathbf{z}}. \quad (2.3)$$

F^P quantifies the variation in amplitude radiated about the source and is given by

$$\begin{aligned} F^P &= \frac{2(\gamma \cdot \nu)(\gamma \cdot \bar{u})}{\bar{u}} \\ &= \cos \lambda \sin \delta \sin^2 i_\xi \sin 2(\phi - \phi_s) - \cos \lambda \cos \delta \sin 2i_\xi \cos(\phi - \phi_s) + \\ &\quad \sin \lambda \sin 2\delta (\cos^2 i_\xi - \sin^2 i_\xi \sin^2(\phi - \phi_s)) + \\ &\quad \sin \lambda \cos 2\delta \sin 2i_\xi \sin(\phi - \phi_s), \end{aligned} \quad (2.4)$$

for a shear dislocation.

$i_\xi, \lambda, \delta, \phi_s, \phi$ represent the take-off angle, slip, dip, strike, of the fault plane, and azimuth to the receiver location, respectively, as displayed in Figure 2.1.

Regrouping equation (2.4) about like coefficients of i_ξ gives

$$\begin{aligned}
 F^P &= \frac{2(\gamma \cdot \nu)(\gamma \cdot \bar{u})}{\bar{u}} \\
 &= [\cos \lambda \sin \delta \sin 2(\phi - \phi_s) - \sin \lambda \sin 2\delta \sin^2(\phi - \phi_s)] \sin^2 i_\xi + \\
 &\quad [\sin \lambda \cos 2\delta \sin(\phi - \phi_s) - \cos \lambda \cos \delta \cos(\phi - \phi_s)] \sin 2i_\xi + \\
 &\quad [\sin \lambda \sin 2\delta] \cos^2 i_\xi.
 \end{aligned} \tag{2.5}$$

Using (2.5), we can now show that the *P-wave* displacement, caused by an arbitrary source orientation can be written as a weighted sum of three fundamental mechanisms.

First let $\lambda = 0^\circ, \delta = 90^\circ$ and $\phi - \phi_s = 45^\circ$. Inserting these into equation (2.2) gives:

$$\mathbf{u}^P(\mathbf{x}, t)|_{\lambda=0^\circ, \delta=90^\circ, \phi-\phi_s=45^\circ} = \sin^2 i_\xi G \bar{u}(t - \frac{r}{\alpha}) \hat{\mathbf{l}}. \tag{2.6}$$

Next let $\lambda = 90^\circ, \delta = 90^\circ$ and $\phi - \phi_s = 90^\circ$. Inserting these into equation (2.2) gives:

$$\mathbf{u}^P(\mathbf{x}, t)|_{\lambda=90^\circ, \delta=90^\circ, \phi-\phi_s=90^\circ} = \sin 2i_\xi G \bar{u}(t - \frac{r}{\alpha}) \hat{\mathbf{l}}. \tag{2.7}$$

Finally, let $\lambda = 90^\circ, \delta = 45^\circ$ and $\phi - \phi_s = 0^\circ$. Inserting these into equation (2.2) gives:

$$\mathbf{u}^P(\mathbf{x}, t)|_{\lambda=90^\circ, \delta=45^\circ, \phi-\phi_s=0^\circ} = \cos^2 i_\xi G \bar{u}(t - \frac{r}{\alpha}) \hat{\mathbf{l}}. \tag{2.8}$$

We can, therefore, rewrite $\mathbf{u}^P(\mathbf{x}, t)$ for an arbitrary source as

$$\begin{aligned}
\mathbf{u}^P(\mathbf{x}, t) = & \\
& [\cos \lambda \sin \delta \sin 2(\phi - \phi_s) - \sin \lambda \sin 2\delta \sin^2(\phi - \phi_s)] \mathbf{u}^P(\mathbf{x}, t)|_{0^\circ, 90^\circ, 45^\circ} + \\
& [\sin \lambda \cos 2\delta \sin(\phi - \phi_s) - \cos \lambda \cos \delta \cos(\phi - \phi_s)] \mathbf{u}^P(\mathbf{x}, t)|_{90^\circ, 90^\circ, 90^\circ} + \\
& [\sin \lambda \sin \delta] \mathbf{u}^P(\mathbf{x}, t)|_{90^\circ, 45^\circ, 0^\circ}. \tag{2.9}
\end{aligned}$$

In terms of moment tensor components, equation (2.9) can be written as

$$\begin{aligned}
\mathbf{u}^P(\mathbf{x}, t) = & [\cos^2 \phi \mathbf{M}_{11} + \sin^2 \phi \mathbf{M}_{22} + \sin 2\phi \mathbf{M}_{12}] \mathbf{u}^P(\mathbf{x}, t)|_{0^\circ, 90^\circ, 45^\circ} \\
& + [(\cos \phi \mathbf{M}_{13} + \sin \phi \mathbf{M}_{23})] \mathbf{u}^P(\mathbf{x}, t)|_{90^\circ, 90^\circ, 90^\circ} \\
& + [\mathbf{M}_{33}] \mathbf{u}^P(\mathbf{x}, t)|_{90^\circ, 45^\circ, 0^\circ}, \tag{2.10}
\end{aligned}$$

where the moment tensor components are defined as:

$$\begin{aligned}
\mathbf{M}_{11} &= -M_o(\sin \lambda \cos \delta \sin 2\phi_s + \sin \lambda \sin 2\delta \sin^2 \phi_s) \\
\mathbf{M}_{12} &= M_o(\sin \lambda \cos \delta \cos 2\phi_s + \sin \lambda \cos 2\delta \sin \phi_s) \\
\mathbf{M}_{13} &= -M_o(\cos \lambda \cos \delta \cos \phi_s + \frac{1}{2} \sin \lambda \sin 2\delta \sin 2\phi_s) \\
\mathbf{M}_{22} &= M_o(\sin \delta \cos \lambda \sin 2\phi_s - \sin 2\delta \sin \lambda \cos^2 \phi_s) \\
\mathbf{M}_{23} &= -M_o(\cos \delta \cos \lambda \sin \phi_s - \cos 2\delta \sin \lambda \cos \phi_s) \\
\mathbf{M}_{33} &= M_o(\sin 2\delta \sin \lambda). \tag{2.11}
\end{aligned}$$

Figure 2.2 shows the amplitude of the *P-wave* radiation pattern for a vertical strike-slip fault.

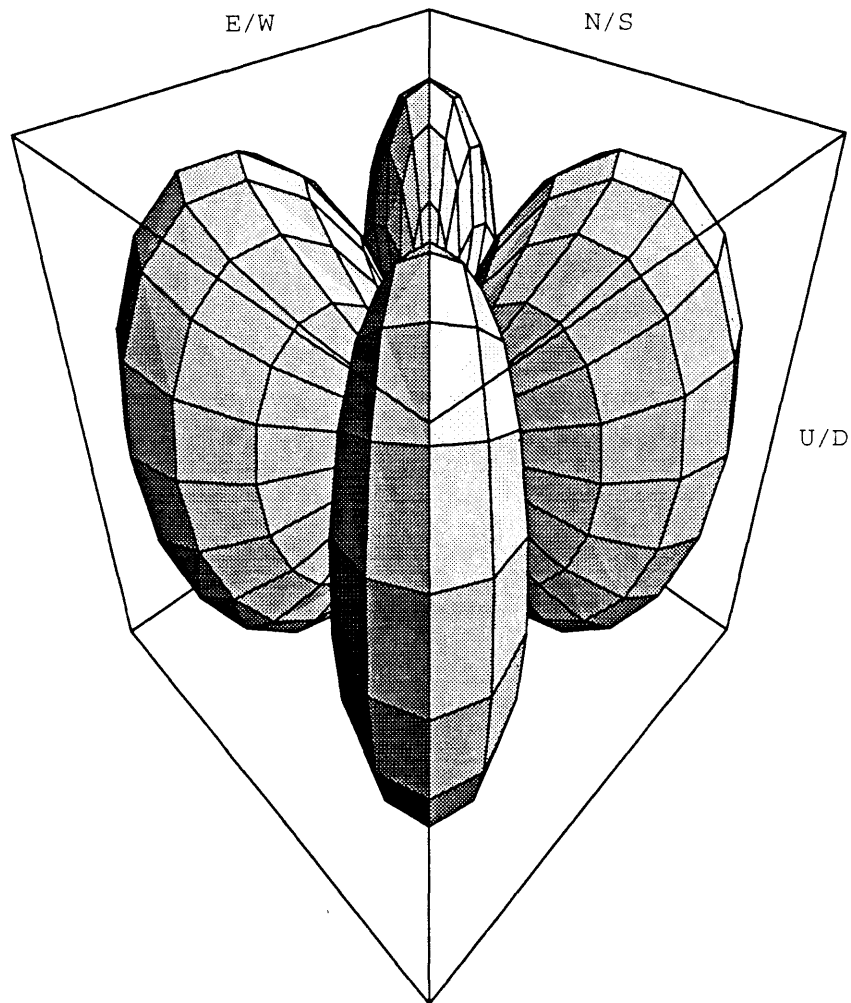


Figure 2.2: *P-wave* radiation pattern for a vertical strike slip fault.

2.2 SV-wave

Similar equations can be derived for *SV* and *SH-waves*. From Aki and Richards (1980), the far-field *SV-wave* displacement is given by

$$\mathbf{u}^{SV}(\mathbf{x}, t) = \frac{F^{SV} \mu A}{4\pi\beta^3 r \rho} \bar{u}\left(t - \frac{r}{\beta}\right) \hat{\mathbf{p}}. \quad (2.12)$$

Let

$$G = \frac{\mu A}{4\pi\beta^3 r \rho},$$

then

$$\mathbf{u}^{SV}(\mathbf{x}, t) = F^{SV} G \bar{u}\left(t - \frac{r}{\beta}\right) \hat{\mathbf{p}}, \quad (2.13)$$

where

β is *SV-wave* velocity, $\hat{\mathbf{p}}$ is direction cosine of *SV-wave*

$$\hat{\mathbf{p}} = \cos i_\xi \cos \phi \hat{\mathbf{x}} + \cos i_\xi \sin \phi \hat{\mathbf{y}} - \sin i_\xi \hat{\mathbf{z}}. \quad (2.14)$$

The *SV-wave* radiation pattern is given by,

$$\begin{aligned} F^{SV} &= \frac{[(\gamma \cdot \nu)(\bar{u} \cdot \hat{\mathbf{p}}) + (\gamma \cdot \bar{u})(\nu \cdot \hat{\mathbf{p}})]}{\bar{u}} \\ &= \sin \lambda \cos 2\delta \cos 2i_\xi \sin(\phi - \phi_s) - \cos \lambda \cos \delta \cos 2i_\xi \cos(\phi - \phi_s) + \\ &\quad \frac{1}{2} \cos \lambda \sin \delta \sin 2i_\xi \sin 2(\phi - \phi_s) - \\ &\quad \frac{1}{2} \sin \lambda \sin 2\delta \sin 2i_\xi (1 + \sin^2(\phi - \phi_s)). \end{aligned} \quad (2.15)$$

We can write (2.12) in terms of moment tensor components and regroup about i_ξ

$$\begin{aligned} \mathbf{u}^{SV}(\mathbf{x}, t) = & [\cos^2 \phi \mathbf{M}_{11} + \sin^2 \phi \mathbf{M}_{22} + \sin 2\phi \mathbf{M}_{12}] \sin 2i_\xi \\ & + [\cos \phi \mathbf{M}_{13} + \sin \phi \mathbf{M}_{23}] \cos 2i_\xi \end{aligned} \quad (2.16)$$

Using (2.16), we can now show that the *SV-wave* displacement caused by an arbitrary source mechanism can be written as a weighted sum of two fundamental sources. First let $\lambda = 0^\circ$, $\delta = 90^\circ$ and $\phi - \phi_s = 45^\circ$. Inserting these into equation (2.12) gives:

$$\mathbf{u}^{SV}(\mathbf{x}, t)|_{\lambda=0^\circ, \delta=90^\circ, \phi-\phi_s=45^\circ} = \frac{1}{2} \sin^2 i_\xi G \bar{u}(t - \frac{r}{\alpha}) \hat{\mathbf{p}} \quad (2.17)$$

Next let $\lambda = 90^\circ$, $\delta = 90^\circ$ and $\phi - \phi_s = 90^\circ$. Inserting these into equation (2.12) gives:

$$\mathbf{u}^{SV}(\mathbf{x}, t)|_{\lambda=90^\circ, \delta=90^\circ, \phi-\phi_s=90^\circ} = -\sin 2i_\xi G \bar{u}(t - \frac{r}{\alpha}) \hat{\mathbf{p}} \quad (2.18)$$

We can now write $\mathbf{u}^{SV}(\mathbf{x}, t)$ for an arbitrary source as

$$\begin{aligned} \mathbf{u}^{SV}(\mathbf{x}, t) = & [\cos^2 \phi \mathbf{M}_{11} + \sin^2 \phi \mathbf{M}_{22} + \sin 2\phi \mathbf{M}_{12}] \mathbf{u}^{SV}(\mathbf{x}, t)|_{0^\circ, 90^\circ, 45^\circ} \\ & + [(\cos \phi \mathbf{M}_{13} + \sin \phi \mathbf{M}_{23})] \mathbf{u}^{SV}(\mathbf{x}, t)|_{90^\circ, -90^\circ, 90^\circ} \end{aligned} \quad (2.19)$$

Note that equation (2.10) and equation (2.19) have the same fundamental Green's functions for *P* and *SV waves*.

Figure 2.3 shows *SV-wave* radiation pattern for a vertical strike-slip fault.

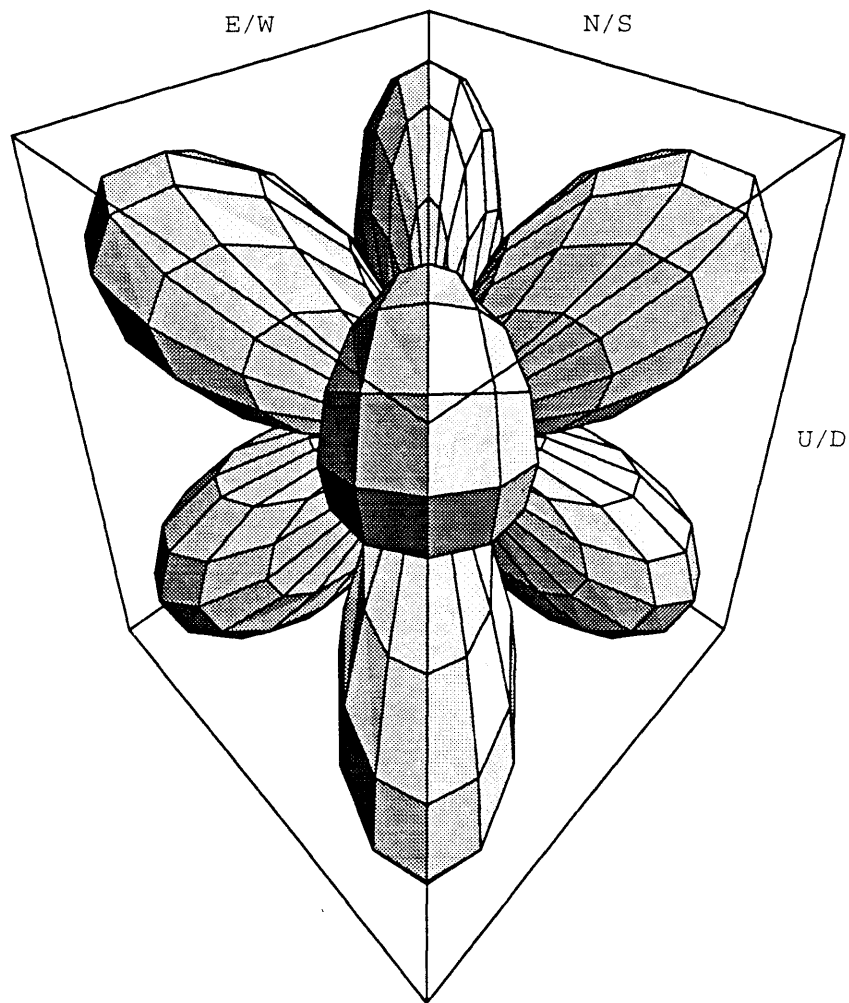


Figure 2.3: *SV-wave* radiation pattern for a vertical strike slip fault.

2.3 SH-wave

Finally, the far field displacement for *SH-waves* is given by

$$\mathbf{u}^{SH}(\mathbf{x}, t) = \frac{F^{SH} \mu A}{4\pi\beta^3 r \rho} \bar{u}(t - \frac{r}{\beta}) \hat{\phi}. \quad (2.20)$$

Let

$$G = \frac{\mu A}{4\pi\beta^3 r \rho},$$

then

$$\mathbf{u}^{SH}(\mathbf{x}, t) = F^{SH} G \bar{u}(t - \frac{r}{\beta}) \hat{\phi}, \quad (2.21)$$

where, β is *SH-wave* velocity and $\hat{\phi}$ is direction cosine of *SH-wave* given by

$$\hat{\phi} = -\sin \phi \hat{\mathbf{x}} + \cos \phi \hat{\mathbf{y}}. \quad (2.22)$$

$$\begin{aligned} F^{SH} &= \frac{[(\gamma \cdot \nu)(\bar{u} \cdot \hat{\phi}) + (\gamma \cdot \bar{u})(\nu \cdot \hat{\phi})]}{\bar{u}} \\ &= \cos \lambda \cos \delta \cos i_\xi \sin(\phi - \phi_s) + \cos \lambda \sin \delta \sin i_\xi \cos 2(\phi - \phi_s) + \\ &\quad \sin \lambda \cos 2\delta \cos i_\xi \cos(\phi - \phi_s) - \\ &\quad \frac{1}{2} \sin \lambda \sin 2\delta \sin i_\xi \sin 2(\phi - \phi_s). \end{aligned} \quad (2.23)$$

To calculate the fundamental seismograms for *SH-waves*, let

$$\lambda = -90^\circ, \delta = -90^\circ \text{ and } \phi - \phi_s = 0^\circ,$$

then

$$\mathbf{u}^{SH}(\mathbf{x}, t)|_{90^\circ, -90^\circ, 45^\circ} = \cos i_\xi G \bar{u}(t - \frac{r}{\alpha}) \hat{\phi}. \quad (2.24)$$

Next, let

$$\lambda = 0^\circ, \delta = -90^\circ \text{ and } \phi - \phi_s = 0^\circ,$$

then

$$\mathbf{u}^{SH}(\mathbf{x}, t)|_{0^\circ, -90^\circ, 0^\circ} = \sin i_\xi G \bar{u}(t - \frac{r}{\alpha}) \hat{\phi}. \quad (2.25)$$

The *SH-wave* displacement can be written in terms of these fundamental seismograms and moment tensor components as,

$$\begin{aligned} \mathbf{u}^{SH}(\mathbf{x}, t) = & \left[\frac{1}{2} \sin 2\phi (\mathbf{M}_{22} - \mathbf{M}_{11}) + \cos 2\phi \mathbf{M}_{12} \right] \mathbf{u}^{SH}(\mathbf{x}, t)|_{90^\circ, -90^\circ, 45^\circ} \\ & + [\cos \phi \mathbf{M}_{23} - \sin \phi \mathbf{M}_{13}] \mathbf{u}^{SH}(\mathbf{x}, t)|_{0^\circ, -90^\circ, 0^\circ} \end{aligned} \quad (2.26)$$

Figure 2.4 shows the *SH-wave* radiation pattern for a vertical strike-slip fault.

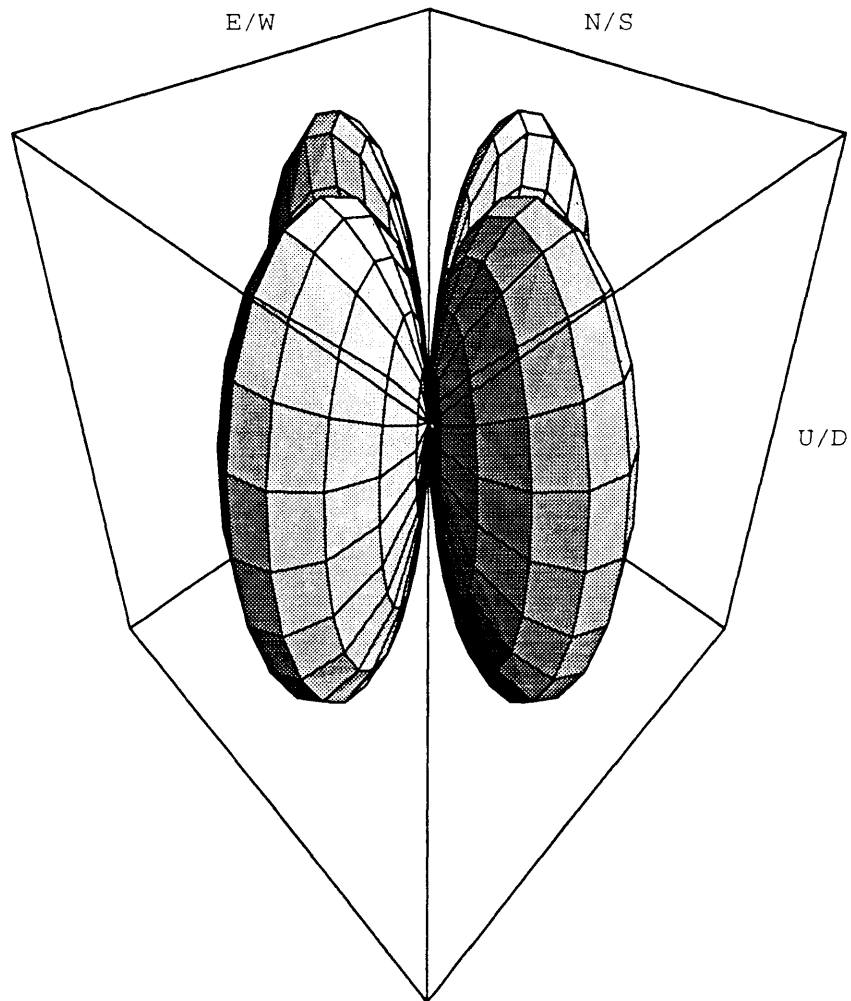


Figure 2.4: *SH-wave* radiation pattern for a vertical strike slip fault.

Chapter 3

REFLECTIVITY METHOD

3.1 Introduction

Methods to synthesize seismic waveforms can generally be classified into two main groups: generalized ray and complete solution methods. Generalized ray methods use a limited approximation of the seismic wavefield. Mostly, they are used for synthesizing either a small part of the seismogram or for estimating the general behaviour of the major seismic phases. The Cagniard technique used by Helmberger (1974) gives good results if sufficient reflections in the layer are included. The WKBJ technique introduced by Chapman (1978) provides an economical technique applicable to a smoothly varying velocity model. This is a good way to determine the main character of the wavefield, but for waves interacting with interfaces at near grazing incidence or in the presence of shadow zones the WKBJ method gives significant errors (Chapman and Orcutt, 1985). The main difference between the two methods comes from the way of using the transformed wave equation and calculating the two

inverse transform integrals. In the case of the generalized ray methods (Helmberger 1974), the inverse transform integral is performed analytically by approximating the integrand function with an appropriate asymptotic expansion. The result is then a decomposition of the complete solution in terms of rays. Complete solution techniques use a complete solution of the double transformed wave equation by allowing for all possibilities of *P*- and *S*-wave propagation throughout the structural model by treating it as a boundary value problem (Fucsh and Muller, 1971). Application of the generalized ray method requires the specification of ray paths and the solution is obtained only for those predefined rays. The complete solution methods need only the structural model and frequency bandwidth. Partial responses can be obtained by specifying a ray parameter window and multiple reflections can be ignored (Kennett, 1983). The main disadvantage of the complete solution techniques when compared to the generalized ray techniques is that they are computationally expensive and identification of the phases on the synthetics may not be clear.

The reflectivity method is a complete solution technique which has been widely used for the computation of synthetic seismograms. The original reflectivity method developed by Fucsh and Muller (1971) required the source and receiver to be above the reflection zone and it included no free surface. Kennett (1983), however, extended the method to calculate the complete earth response for any source receiver location. The original reflectivity method involves the computation of the reflectivity function

and the double transformation of that function from frequency-slowness space. In order to avoid aliasing, the reflectivity function must be adequately sampled. This is computationally expensive. Friyer (1980) introduced the method by integrating first over frequency then over slowness in contrast to the conventional spectral method of integrating over slowness then over frequency.

3.2 Method

The model used to develop the reflectivity method is shown in Figure 3.1. It consists of $n-1$, plane homogenous and isotropic layers on top of a half space. The layers are characterized by α , P -wave velocity, β , S -wave velocity, and ρ , density.

The core of the computation of the reflectivity method is to calculate the overall reflectivity matrix that has a form:

$$\mathbf{R}^- = \begin{pmatrix} RR^d_{PP} & RR^d_{SP} \\ RR^d_{PS} & RR^d_{SS} \end{pmatrix} \quad (3.1)$$

$$\mathbf{R}^+ = \begin{pmatrix} RR^u_{PP} & RR^u_{SP} \\ RR^u_{PS} & RR^u_{SS} \end{pmatrix} \quad (3.2)$$

In (3.1) and (3.2) the negative superscript stands for the bottom (i.e. $z > z_m$) layered half space while the positive superscript indicates the top ($z \leq z_m$); a d stands for all downgoing waves and a u means all upgoing waves; a PP subindex means P to P reflections while PS stands for P to S; S to S and S to P follow the same notation.

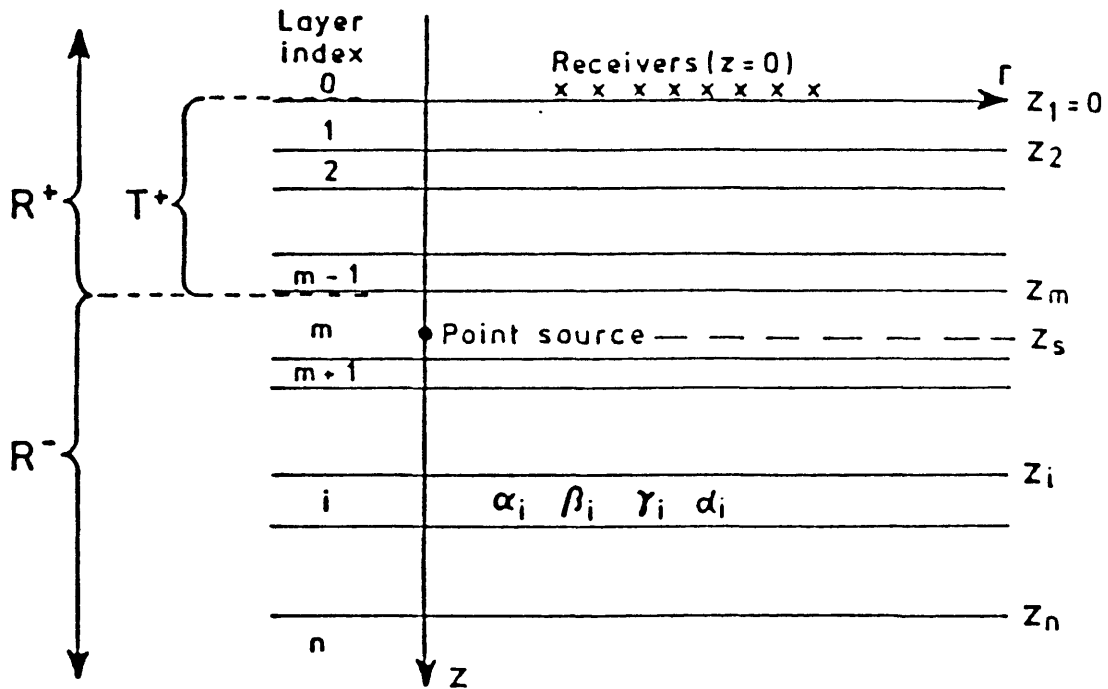


Figure 3.1: Layered medium and equation parameters. The source is located at z_s under the z_m interface. Layer parameters are: $\alpha_i = P$ velocity, $\beta_i = S$ velocity, $\gamma_i =$ density, $d_i =$ thickness, z_i depth to the top. From Kind (1985).

The elements of the matrices in equation (3.1) and (3.2) are derived from a combination of the reflection and transmission coefficients of each one of the interfaces in the respective half space. Their evaluation is performed through a recursive algorithm which propagates the response of one layer to the next until the level opposite to that which contain the source is reached. Hence, the case of the upper half space is treated as that of an incident wavefrom below while the case of the bottom half space is treated as one of the incident from above.

The solution for the displacement field at the surface (i.e at $z = 0$) can be divided into two steps. The first step is the determination of the complete upgoing wavefield in the layer containing the source. The field is the sum of direct upgoing waves and all possible reflections and multiples at the layer stacks above and below the level $z = z_m$ in layer m . All these contributions are expressed as integrals over slowness with a general form:

$$4\pi\rho_m\phi^u = \int_0^\infty (\epsilon_1 B_1 J_0 + \epsilon_2 B_2 J_1) e^{j\omega a_m(z-z_m)} du \quad (3.3)$$

$$4\pi\rho_m\psi^u = \int_0^\infty \frac{1}{ju\omega} (\epsilon_1 D_1 J_0 + \epsilon_2 D_2 J_1) e^{j\omega b_m(z-z_m)} du \quad (3.4)$$

ϕ_u and ψ_u are the upgoing dilatational and rotational potentials, $B_{1,2}$ and $D_{1,2}$ are the displacement potential amplitudes for P and SV , $J_{0,1}$ are Bessel functions of integer of order 0,1, and a_m is the vertical slowness defined as

$$a_m = \left(\frac{1}{\alpha_m^2} - u^2\right)^{1/2}, \quad (3.5)$$

$$b_m = \left(\frac{1}{\beta_m^2} - u^2 \right)^{1/2}, \quad (3.6)$$

where u is the horizontal slowness, ϵ_1 and ϵ_2 are the components of a single force at depth z_s which is harmonic in time and has frequency components F_1, F_2, F_3 .

The displacement potential amplitudes in (3.3) and (3.4) are usually combined in displacement amplitude vectors of the form:

$$\mathbf{V}_{1,2} = \begin{pmatrix} B_{1,2} \\ D_{1,2} \end{pmatrix} \quad (3.7)$$

The amplitude vectors in turn are the terms which contain a combination of the reflectivity matrices operated on the source amplitudes as for example:

$$\begin{aligned} \mathbf{V}_{1,2} &= (\mathbf{I} + \mathbf{R}^- \mathbf{R}^+ + \mathbf{R}^- \mathbf{R}^+ \mathbf{R}^- \mathbf{R}^+) (S^u_{1,2} + \mathbf{R}^- S^d_{1,2}) \\ &= [\mathbf{I} - \mathbf{R}^- \mathbf{R}^+]^{-1} (S^u_{1,2} + \mathbf{R}^- S^d_{1,2}) \end{aligned} \quad (3.8)$$

where $S^{d,u}_{1,2}$ are the source amplitude vectors. These terms then account for the direct wave field and all multiple reflections.

The second step involves the computation of potentials for the upper half space of the layered medium using equations (3.3) and (3.4) and from these, the determination of the displacement components at $z = 0$. These potentials have a form similar to equations (3.3) and (3.4):

$$4\pi\rho_m\phi^0 = \int_0^\infty (\epsilon_1 B_1^0 J_0 + \epsilon_2 B_2^0 J_1) e^{j\omega a_0 z} du \quad (3.9)$$

$$4\pi\rho_m\psi^0 = \int_0^\infty \frac{1}{ju\omega}(\epsilon_1 D_1^0 J_0 + \epsilon_2 D_2^0 J_1)e^{j\omega b_0 z} du \quad (3.10)$$

with the amplitude vectors for *P-SV*:

$$\mathbf{V}_0^{1,2} = \begin{pmatrix} B^0_{1,2} \\ D^0_{1,2} \end{pmatrix} \quad (3.11)$$

The vertical displacement is calculated by inserting equations (3.9) and (3.10) into

$$u_z = \phi_{,z} + \psi_{,rr} - \frac{1}{r}\psi_{,r} - \frac{1}{r^2}\psi_{,\Phi\Phi} \quad (3.12)$$

then

$$4\pi\rho_m u_z = \omega \sum_{i=1}^2 \epsilon_i \int_0^\infty \mathbf{J}_i \mathbf{U} \mathbf{T}^+ \mathbf{V}_i du. \quad (3.13)$$

where

$$\mathbf{U} = \begin{pmatrix} u & b_0 \\ a_0 & -u \end{pmatrix},$$

$$\mathbf{J}_1 = \begin{pmatrix} -J_1(u\omega r) & 0 \\ 0 & -jJ_0(u\omega r) \end{pmatrix},$$

$$\mathbf{J}_2 = \begin{pmatrix} -J_0(u\omega r) & 0 \\ 0 & -jJ_1(u\omega r) \end{pmatrix},$$

and \mathbf{T}^+ is the transmissivity matrix which has similar derivations as \mathbf{R}^+ .

Time domain seismograms are obtained by computing the Fourier transform of the slowness integral representation of the displacement field at the surface.

The equation (3.13) represents the complete displacement field of the medium, including body and surface waves even when they are derived from body-wave propagation notions. Surface waves are related to the poles of the integrands on the positive real(slowness) u -axis which follow from the dispersion equations:

$$\det [\mathbf{I} - \mathbf{R}^- \mathbf{R}^+]^{-1} = 0, \quad (3.14)$$

for Rayleigh waves and

$$1 - R^- R^+ = 0, \quad (3.15)$$

for Love waves.

Chapter 4

INVERSION OF THE GEOPHYSICAL DATA

4.1 Linear least-squares inversion

The objective of the geophysical inversion is to extract a set of model parameters from an attempted fit of the model response to the observed data. The basic strategy is, therefore, to minimize the errors between the model response and the observations. The model response can be either a linear or nonlinear function of the model parameters, but a nonlinear system with respect to model parameters can be linearized using a Taylor series expansion. The derivation of the least squares inversion techniques is not in the scope of this study, but can be found in Lines and Treitel (1988). The goal is to solve a linear system of equations given by

$$\mathbf{g} = \mathbf{Z}\delta, \tag{4.1}$$

where, \mathbf{g} is the model response and observed data, \mathbf{Z} is Jacobian matrix which contains the partial derivatives of the objective function with respect to model parameters, δ is parameter change vector.

The error vector \mathbf{e} is defined as

$$\mathbf{e} = \mathbf{g} - \mathbf{Z}\delta. \quad (4.2)$$

In the simplest least-squares approach, we seek to minimize the cumulative squared error $S = \mathbf{e}^T \mathbf{e}$ with respect to the parameter change vector. Minimization of S with respect to δ requires that

$$\frac{dS}{d\delta} = 0. \quad (4.3)$$

Carrying out the differentiation to with respect to δ gives a linear system of equations

$$\mathbf{Z}^T \mathbf{Z} \delta = \mathbf{Z}^T \mathbf{g}, \quad (4.4)$$

whose solution for parameter change vector, δ , is

$$\delta = \mathbf{Z}^T \mathbf{Z}^{-1} \mathbf{Z}^T \mathbf{g}. \quad (4.5)$$

When the matrix $\mathbf{Z}^T \mathbf{Z}$ is singular, the difficulties arise finding the inverse. Levenberg (1944) and Marquard (1963) replaced the equation (4.5) with

$$\delta = (\mathbf{Z}^T \mathbf{Z}^{-1} + \theta \mathbf{I}) \mathbf{Z}^T \mathbf{g}, \quad (4.6)$$

where \mathbf{I} is identity matrix and θ is known as Marquard factor which may be adjusted to control iteration step size. If $\theta \rightarrow \infty$, δ tends to $\theta \mathbf{Z}^T \mathbf{g}$ which is an adjustment in the steepest descent direction. If $\theta \rightarrow 0$, δ is the Gauss-Newton adjustment vector. The idea is to guarantee a decrease in the sum of the squares of the residuals via

steepest descent when initial estimate of parameters far from the minimum, and to switch to the rapid convergence of Newton's method as the minimum is approached.

The parameter changes from the initial response estimates are determined by the use of equation (4.6) and an updated set of parameters are obtained to compute the new model response. The iterative search for parameter estimates terminates whenever the RMS error become less than a prespecified value.

4.2 Singular Value Decomposition

The least-square technique may fail when $\mathbf{Z}^T\mathbf{Z}$ and \mathbf{Z}^T is nearly singular. Golub and Reinsch (1970) recognized this problem and developed an efficient algorithm to solve equation (4.1) which makes use of the singular value decomposition(SVD). This procedure factors \mathbf{Z} into a product of three matrices,

$$\mathbf{Z} = \mathbf{U}\mathbf{\Lambda}\mathbf{V}^T, \quad (4.7)$$

where \mathbf{U} is $n \times p$ matrix whose columns consists of n orthonormalized eigenvectors of \mathbf{Z} , \mathbf{V} is $p \times p$ matrix whose columns contain the p orthonormal eigenvectors, and $\mathbf{\Lambda}$ is a $p \times p$ diagonal matrix containing p eigenvalues of \mathbf{Z} . Writing the equation $\mathbf{Z}\delta = \mathbf{g}$ in terms of \mathbf{U} and \mathbf{V} gives,

$$\mathbf{U}\mathbf{\Lambda}\mathbf{V}^T\delta = \mathbf{g}. \quad (4.8)$$

The equation (4.8) is solved for parameter change vector, δ , as,

$$\delta = \mathbf{V}\mathbf{\Lambda}^{-1}\mathbf{U}^T\mathbf{g}. \quad (4.9)$$

The equation (4.6) can be written in terms of decomposition matrices as

$$\delta = \mathbf{V}(\mathbf{\Lambda} + \theta\mathbf{I})^{-1}\mathbf{U}^T\mathbf{g}. \quad (4.10)$$

θ is Marquard's damping factor and it removes singularity when one of the eigenvalues is zero.

Chapter 5

DATA ANALYSIS

5.1 Introduction

Extracting information from observed seismograms requires the development of specific modeling and inversion techniques. These techniques require one to perform forward calculations involving simplifications and assumptions. These simplifications and assumptions must be justified before the results of the inversion can be interpreted. Most of the time, however, these simplifications and assumptions affect the results in poorly understood ways.

For example, the elastic waves generated by a seismic source and recorded by instruments at various azimuths and distances, about the source, propagate through earth materials with spatially varying properties. Recovering the source characteristics from the observed wavefield is an inverse problem. Such an inverse problem requires that one specify an earth model. The success of the inversion depends on the parameterization of the problem, as well as the initial guess, and the assumed

earth model. A homogeneous and isotropically layered earth model can be justified if one is studying long period teleseismic observations. Waveforms recorded at regional distances, however, propagate through a highly heterogeneous crust. A simple layered model of this structure is usually not adequate. This difficulty is fundamental. Even if we could efficiently calculate seismograms for nonhomogeneous, nonisotropic media, rarely would we be able to exactly specify the earth's velocity structure. The best we can do is to try to understand the effects of variations in earth structure on the determination of earthquake source mechanisms and develop parameterizations of the observed wavefield which are not sensitive to structural variations.

5.2 Quantitative analysis of the seismograms

The earth model used in this study (Figure 5.1) represents a simple crustal structure that is characterized by velocity (P and S), density, and the quality factors of the medium (Kind, 1985). To simulate the effect of a laterally varying velocity structure, we perturb the reference model randomly and calculate observed seismograms generated from these perturbed models. Model perturbations are generated assuming a P -wave velocity distributed normally about the reference model with a variance 7%. Aki and Lee (1976) determined 6% high and 15% low velocity perturbations using local earthquakes in California. Lees and Malin (1990) found 10% variations in the velocity derived from the local earthquakes in Washington state. 7%

variation may be a good approximation for the regional distances. *S-wave* velocity is calculated from *P-wave* velocity assuming a Poisson ratio between 0.3-0.4. Density is calculated from the *P-waves* assuming the same ratio as in reference model. For the present study, perturbations do not include layer boundaries or focal depths.

Fundamental seismograms are calculated using the reflectivity technique described in Chapter 3 for both the reference and perturbed models. 5000 slownesses between 0.05-3.0 sec/km, and a 0.05 Hz low-cut and 3.0 Hz high-cut zero phase, 6 pole Butterworth filter is used in the calculation of the fundamental Green's functions. Fundamental Green's functions are calculated at distances of 1000, 1500, 2000 km and a focal depth of 10 km is assumed. Using these fundamental Green's functions, we can calculate seismograms with arbitrarily oriented source mechanisms at any azimuth as described in Chapter 2. Figure 5.2 shows the three vertical component fundamental Green's functions for the earth model shown in Figure 5.1. The beginning portion of the seismograms for strike slip and 45° dipping dip slip mechanisms is dominated by *Pn*, that is a *P-wave* travelling along the top of the mantle as a head wave. The arrivals following *Pn* can be interpreted as *pPn* and *sPn*. Direct *P* arrivals can be seen at the end of *Pn* wave train with higher frequency characteristics. *Sn* follows the direct *P* arrivals and are dominated by lower frequencies. The end of *Sn* arrivals also includes additional *S* phases. *Lr* waves dominate the seismograms with large amplitudes. Seismograms for dip slip source mechanism contains only *Lr*

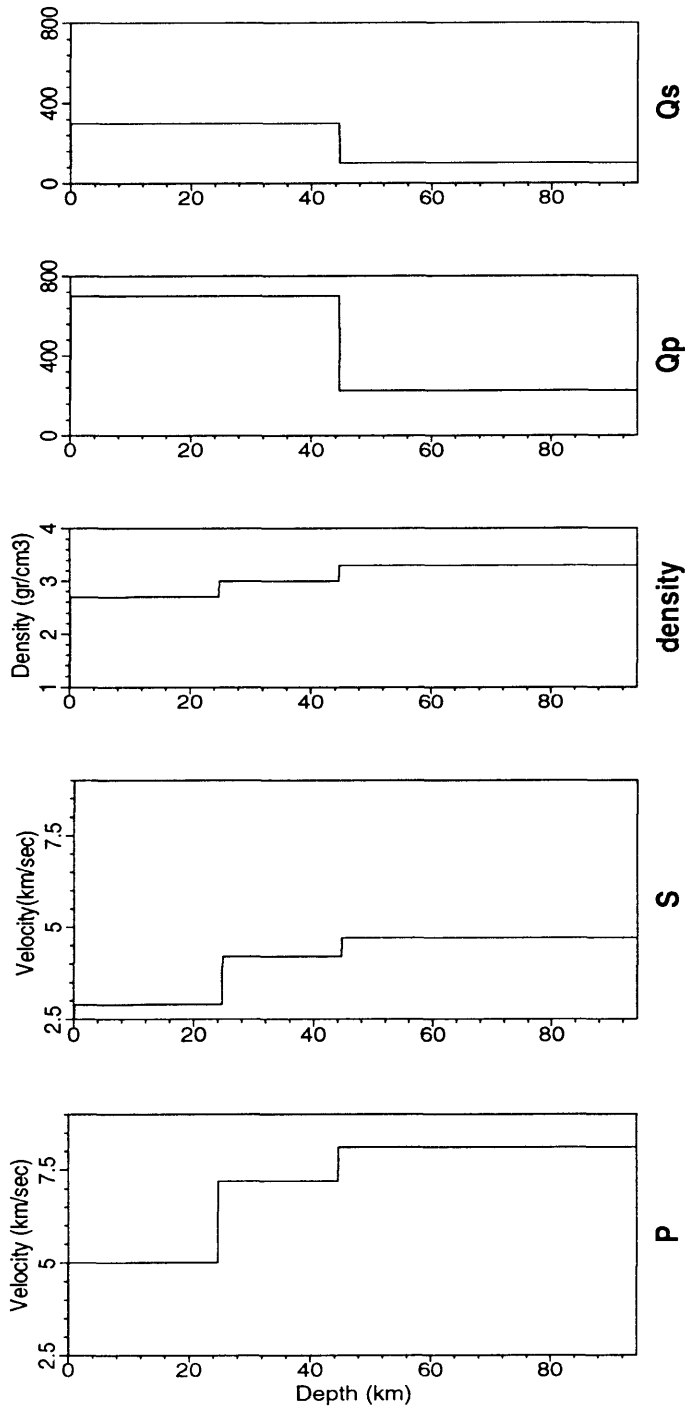


Figure 5.1: Reference Earth model used in the calculation of the fundamental Green's functions. Observed seismograms are calculated using earth models which are random perturbations of the reference models. From Kind(1985).

waves. Figure 5.3 shows two tangential component fundamental Green's functions for the earth model shown in Figure 5.1. The tangential components of the seismograms are much simpler than the vertical components. The early part of the seismograms include S_n arrivals while Lg waves dominate the later parts of the records with larger amplitudes.

The perturbed velocity models affect the shape of the seismograms in different ways. In general, we observe that when the velocities of the perturbed model are much lower than those of the reference model, dispersive Love waves and surface waves are not well developed (Figure 5.4). When the velocities are higher than those of reference model, some higher mode energy is included in the surface waves (Figure 5.5).

5.3 Parameterization of the wavefield

Inversion of seismic data is now routinely applied to earthquakes to determine source parameters from teleseismic observations. Few attempts, however, have been made to estimate source parameters from regional data. Stump and Johnson (1982) developed two inversion techniques for regional waveforms, one formulated in the time domain and the other in the frequency domain. Saikia and Herrmann (1985, 1986) used a moment tensor inversion technique for the interpretation of the observed body wave amplitudes at local distances for two aftershocks of the 1982 Miramichi

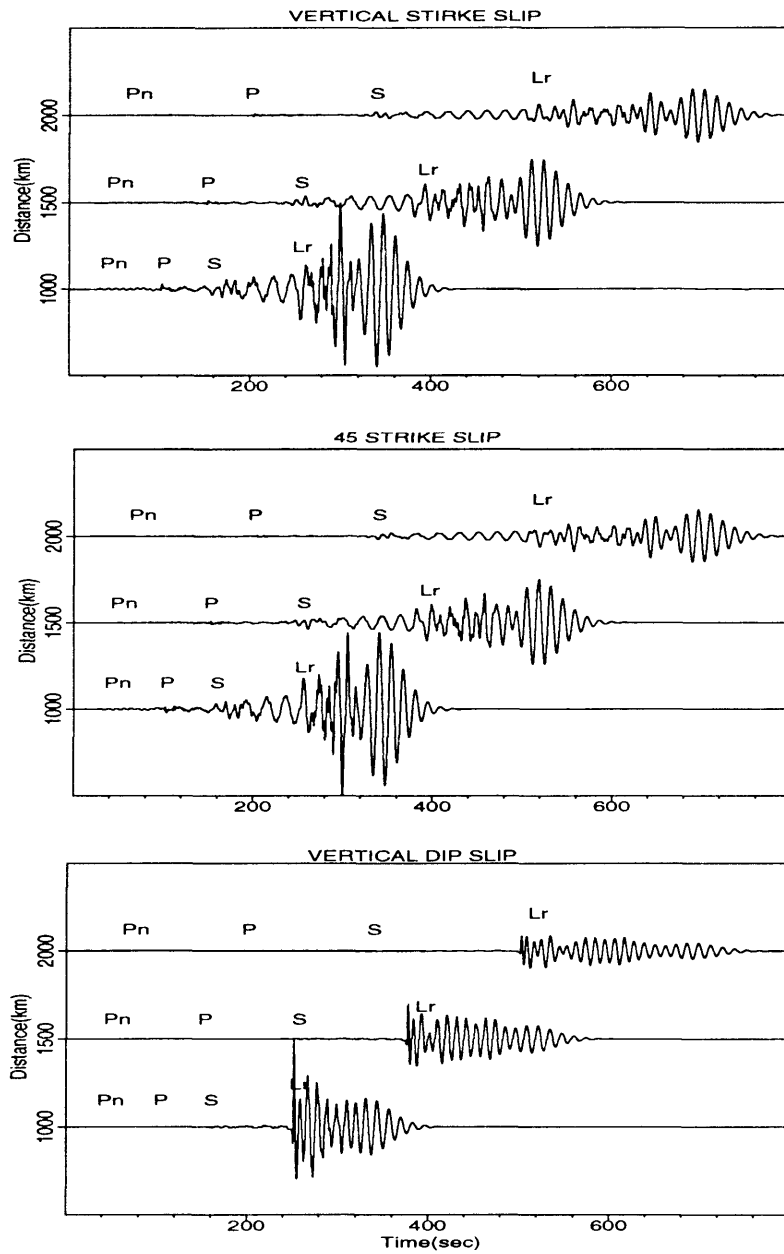


Figure 5.2: Three vertical component fundamental Green's functions. Vertical dip slip is shown on top, vertical strike slip in the middle and 45° dip slip on the bottom.

UNIVERSITY OF CALIFORNIA
SAN DIEGO

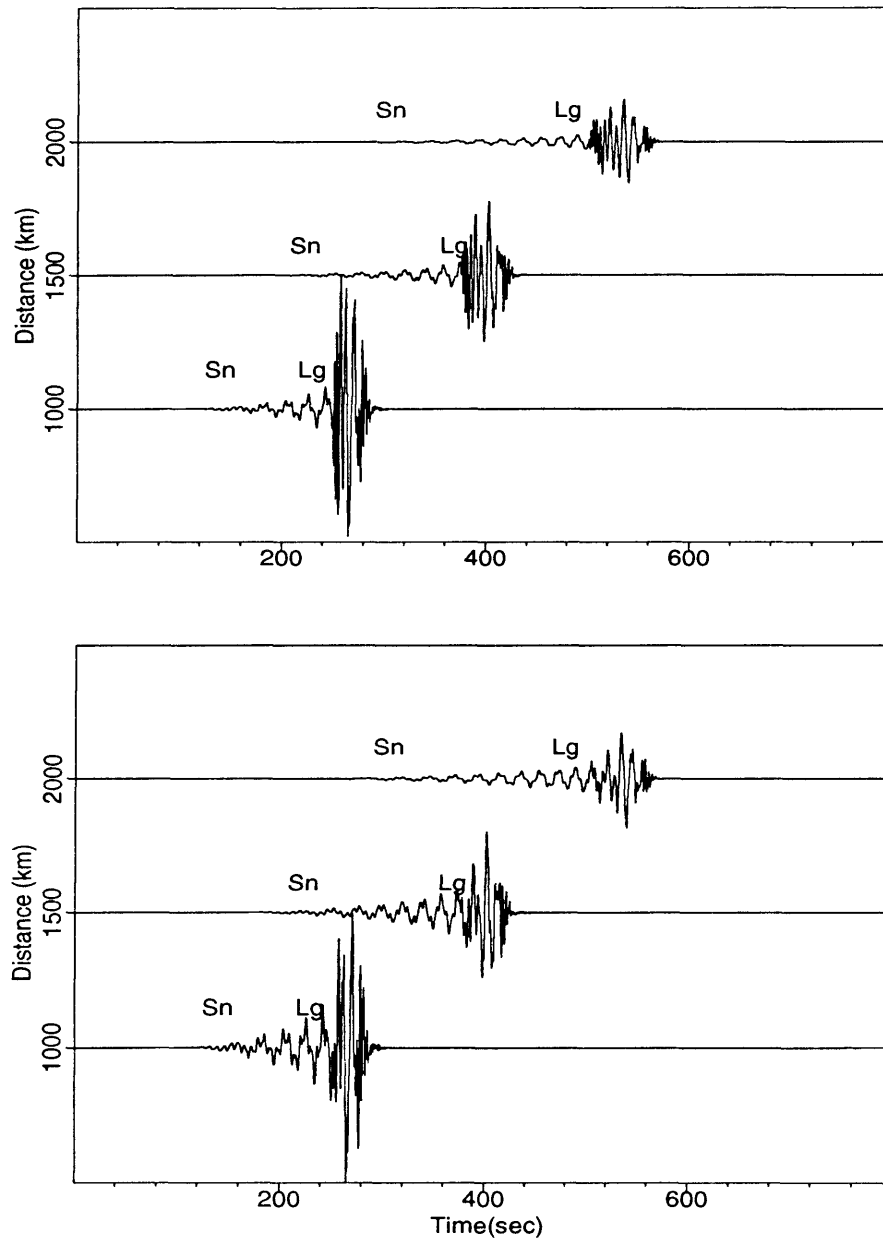


Figure 5.3: Two tangential component fundamental Green's functions. Vertical dip slip is shown on top, 45° dip slip on the bottom.

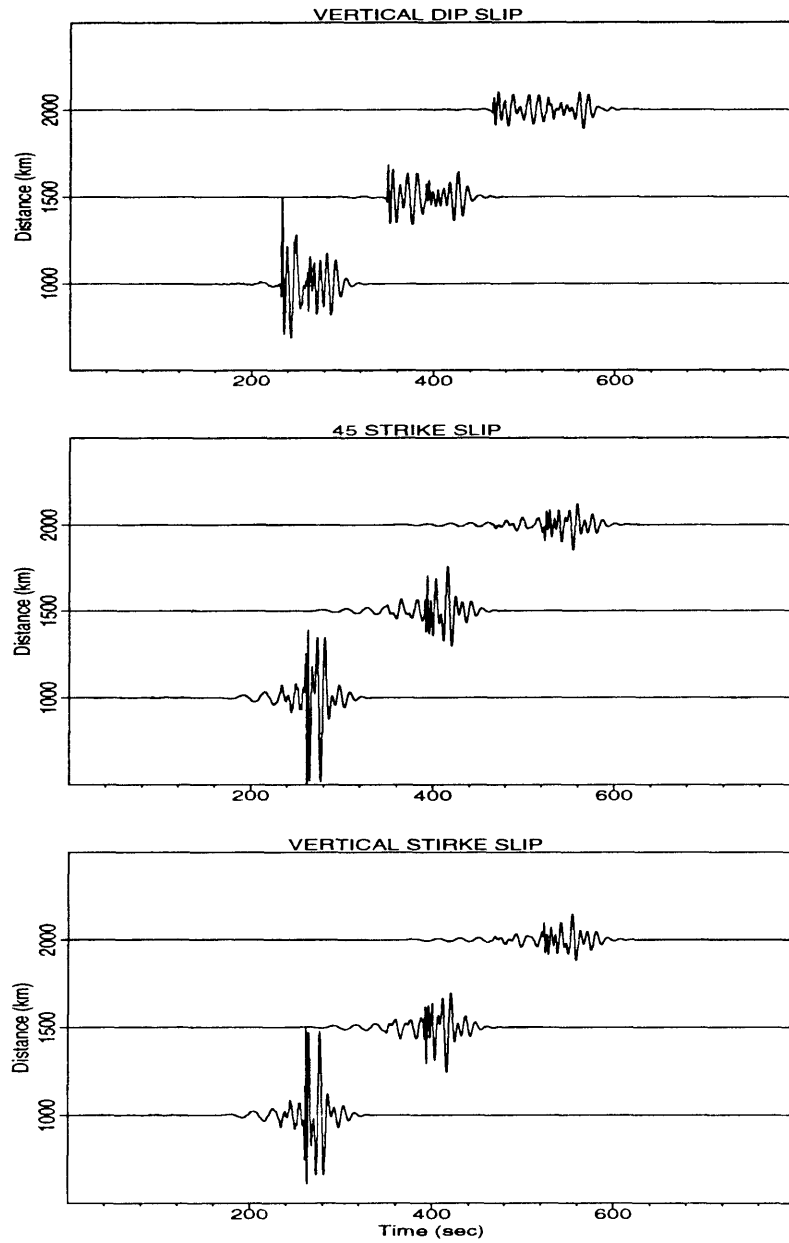


Figure 5.4: Vertical component seismograms for the three fundamental source types calculated for a model with velocities lower than the reference model.

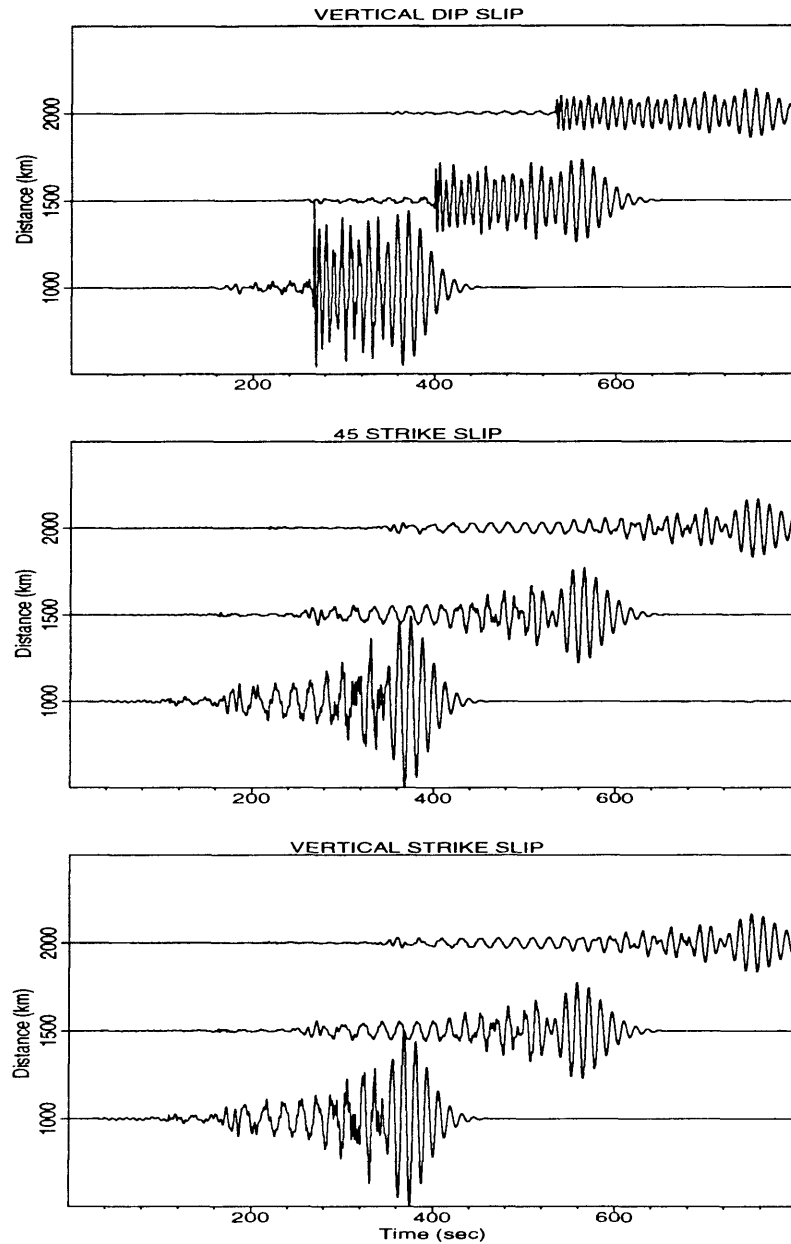


Figure 5.5: Vertical component seismograms for the three fundamental source types calculated for a model with velocities higher than the reference model.

earthquakes and three 1982 Arkansas earthquakes.

As can be seen from the previous figures, reasonable perturbations to the velocity structure can cause large changes in the time domain waveshape. We, therefore, explore parameterizations of the wavefield that average over many time-amplitude observations. These include area, energy and higher order statistical moments of the seismograms and their envelopes.

Consider first, area and energy. The area of a time series is calculated as

$$\int_{t_0}^{t_1} f(t)dt, \quad (5.1)$$

and the energy as

$$\int_{t_0}^{t_1} f(t)^2 dt. \quad (5.2)$$

These parameterizations can be calculated for a specific time window, such as around the P , S , or surface waves, as well as for the entire seismogram.

As a first pass, let us consider the sensitivity of each parameterization to changes in velocity structure. Using seismograms generated from perturbed models and seismograms generated from the reference model, the observed versus calculated parameterizations are plotted and tested for a linear correlation. We will consider correlation coefficients of 0.7 and greater as indicative of parameterizations that insensitive to structural perturbations.

Windowing is crucial in these parameterizations since the arrival times of different phases will be different for seismograms corresponding to different perturbed

models. Each seismogram, therefore, should be windowed separately. S and Love waves arrivals are considered in the same time window as Lg waves.

For one particular model realization, areas of the P -waveforms are shown in Figure 5.6. The correlation coefficient is 0.90. Some of the waveforms used in the calculation are shown on top. The first row includes waveforms from the reference model and waveforms in the second row are from the perturbed models. The similarity between waveform shape is good. Amplitudes, however, can vary considerably. The correlation coefficient is large enough to warrant further consideration.

Figure 5.7 shows variations in areas and the waveforms for the time windows including surface waves and S -waves only. The correlation coefficient is 0.52. One of the reasons for the instability of this parameterization is that the negative and positive values of the waveforms tend to cancel each other. Therefore, source information is lost and resolution is reduced. We will not consider this parameterization further.

Consider next energy of the waveforms. Figure 5.8 shows the energies of the P waveforms. The correlation coefficient is 0.77. The energies of the surface waves, shown in Figure 5.9, are quite robust also with a correlation coefficient 0.97. Both of these parameterizations will be considered further.

Consider next the envelope of the observed seismograms. The parameterization of the envelope that we have chosen to use is to model the first three statistical moments of the envelope. The determination of a seismogram's envelope is given in

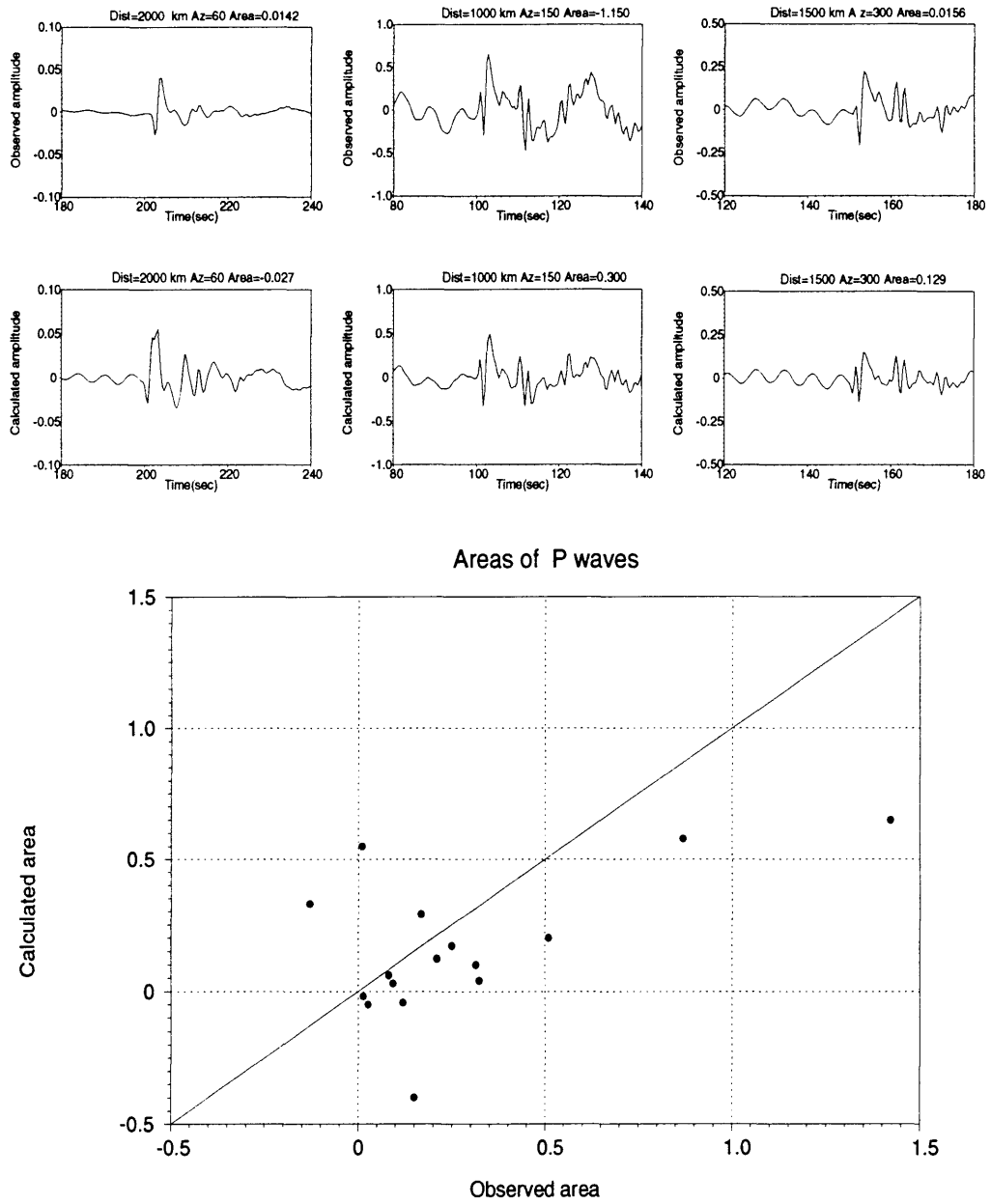


Figure 5.6: Selected observed (first row) and calculated seismograms (second row) for the *P-wave* time window and the correlation between the area of the observed and calculated seismograms. The correlation coefficient is 0.9.

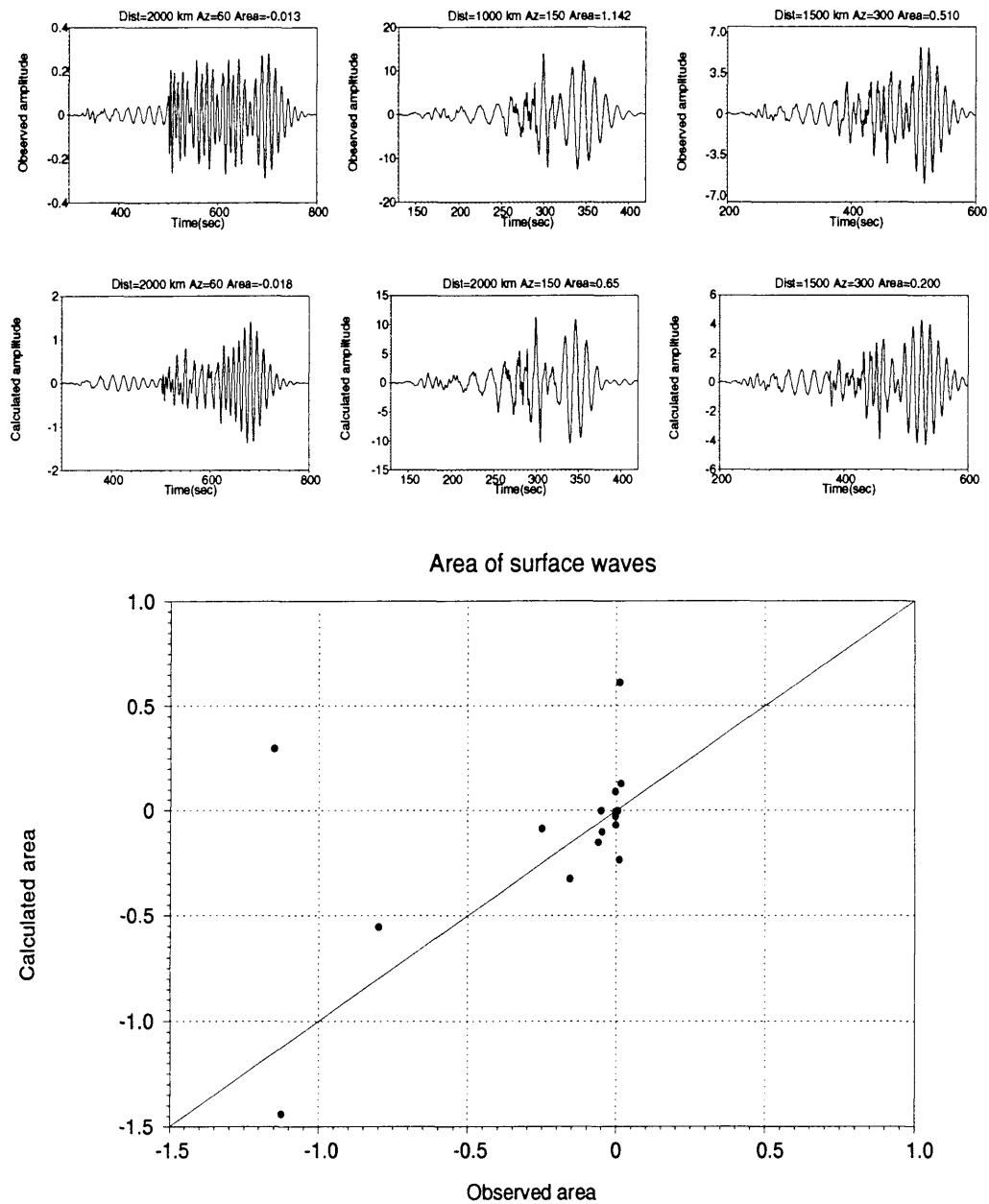


Figure 5.7: Selected observed (first row) and calculated seismograms (second row) for the *surface wave* time window and correlation between the area of the observed and calculated seismograms. The correlation coefficient is 0.52.

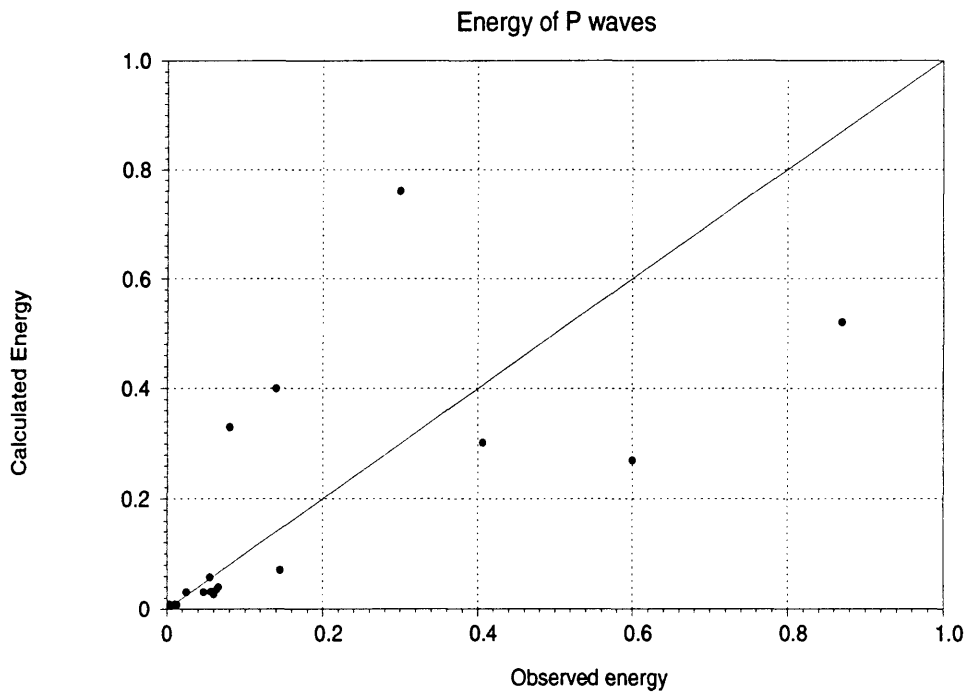
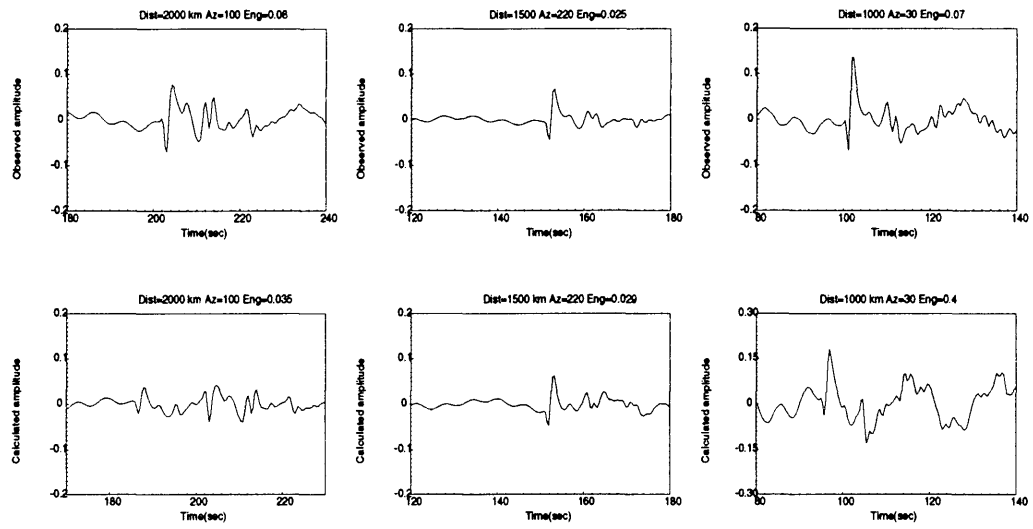


Figure 5.8: Selected observed (first row) and calculated seismograms (second row) for the *P-wave* time window and correlation between the energy of the observed and calculated seismograms. The correlation coefficient is 0.77.

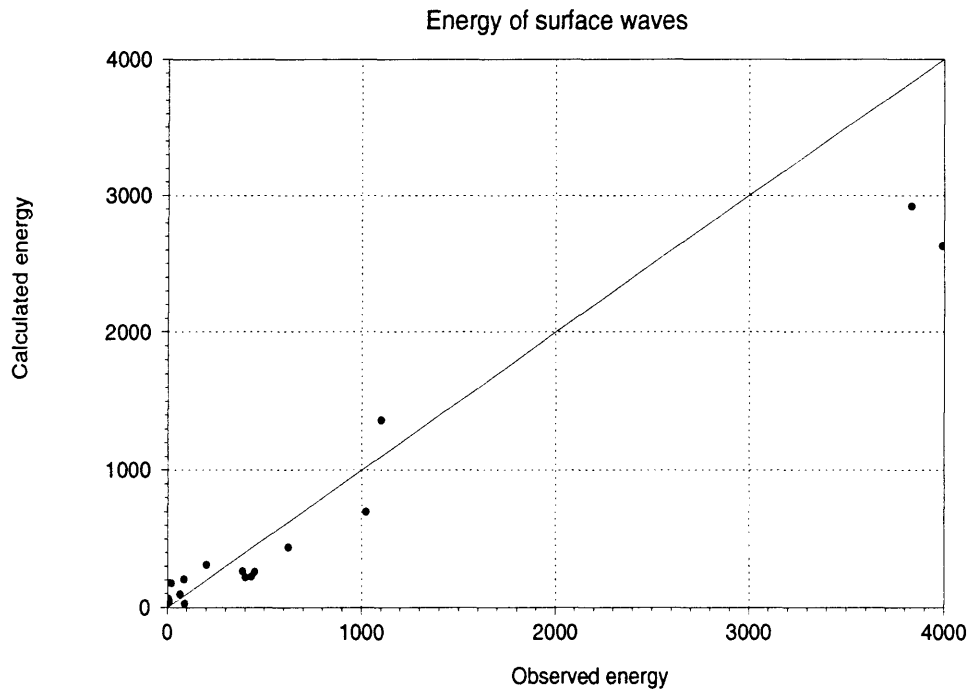
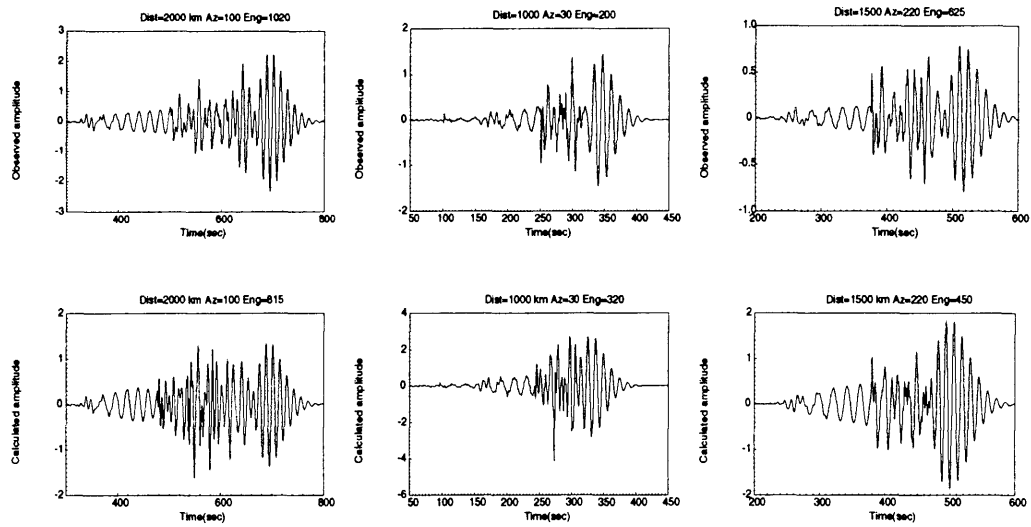


Figure 5.9: Selected observed (first row) and calculated seismograms (second row) for the *surface wave* time window and correlation between the energy of the observed and calculated seismograms. The correlation coefficient is 0.97.

Appendix A. The moments of a function $f(t)$ are defined as

$$\mu_n = \int_{t_0}^{t_1} (t - \mu)^n f(t) dt, \quad (5.3)$$

where μ is centroid of $f(t)$ defined as

$$\mu = \frac{\int_{t_0}^{t_1} t f(t) dt}{\int_{t_0}^{t_1} f(t) dt}. \quad (5.4)$$

In this study, we will only use the first, the second moment, which is variance, and the third moment, which is skewness. Figure 5.10 shows the envelopes of the fundamental seismograms shown in Figure 5.2. To determine the appropriate windowing, the kernel function in equation 5.3, $(t - \mu)^n f(t)$, is plotted versus time for $n=1,2,3$ (Figure 5.11). All curves are scaled to the same level. The important feature to notice is that even though the *P* and *S-wave* amplitudes are very small, they produce a large contribution to the integral given in equation 5.3 since they are far from centroid. This is undesirable since, in the presence of the noise, the earlier part of the envelopes may give large anomalies with small amplitude changes and reduce resolution. Therefore, the time windows used in the calculation of area and energies are also used for this part of the study.

In order to understand the sensitivity of the moments of the envelopes to structural changes we again perform a simple correlation test. Figure 5.12 shows the correlation of the moments between observed and calculated seismograms for the *P-wave* time window. The correlation coefficients for the first, second, and third moments are 0.96, 0.94, 0.68. Figure 5.13 shows the correlation of the moments between

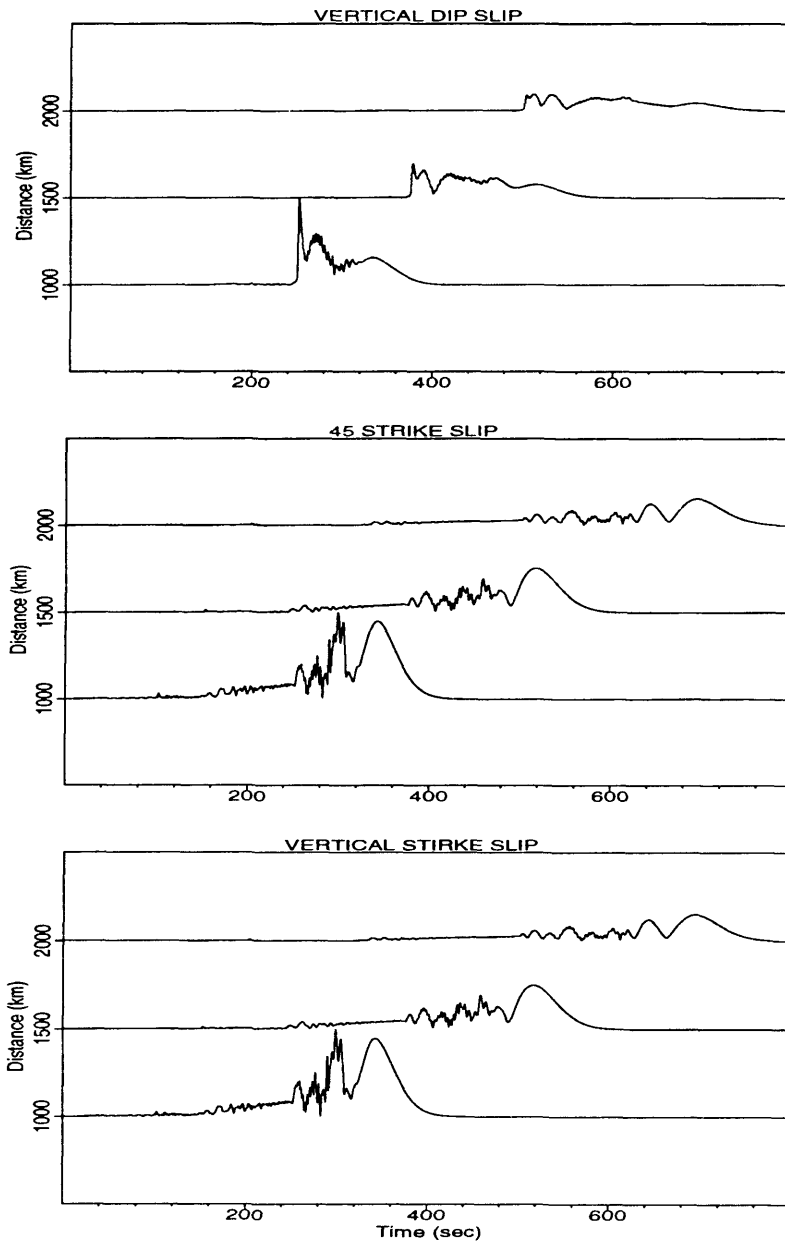


Figure 5.10: Envelopes of the 3 fundamental seismograms shown in Figure 5.2.

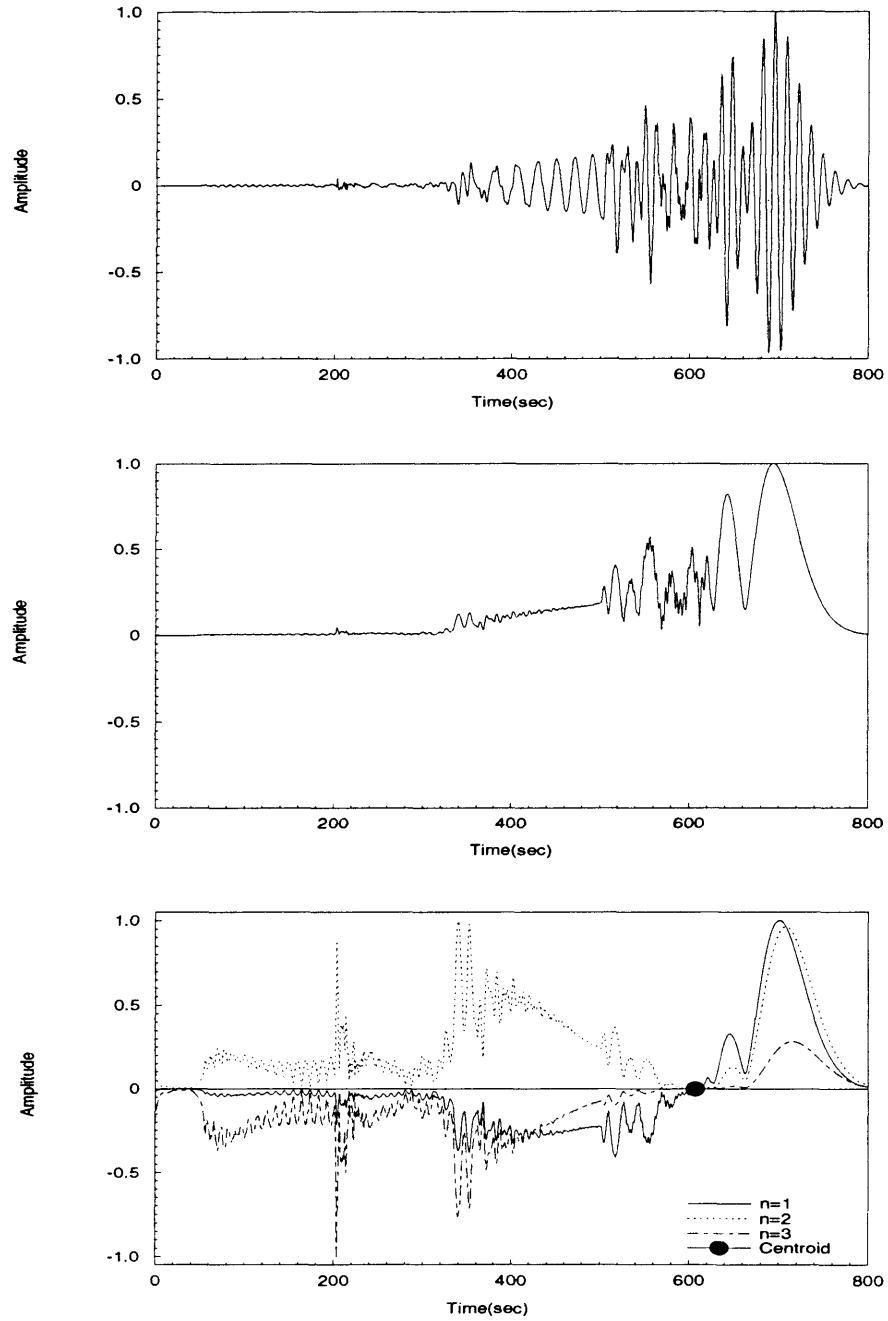
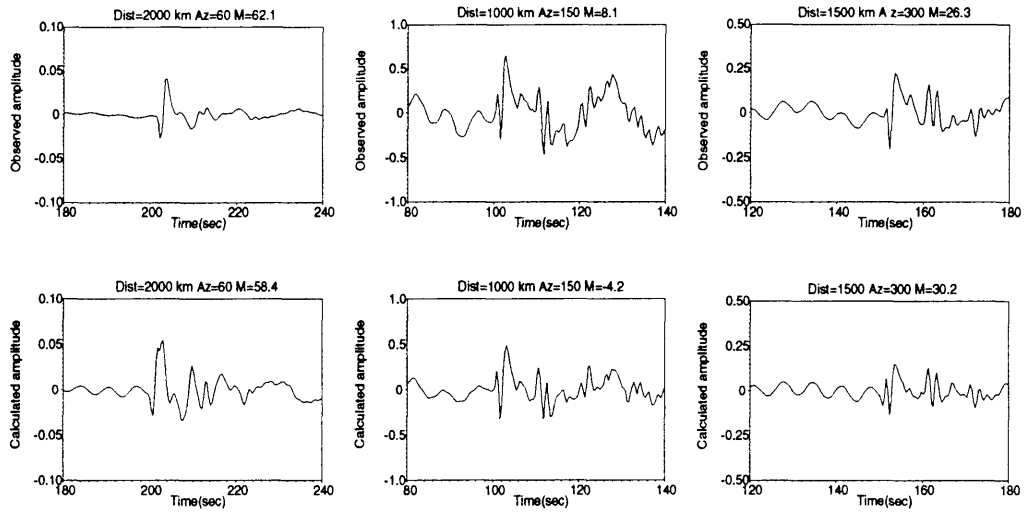


Figure 5.11: Observed seismogram (top), its envelope (middle), and changes in the kernel function of the moments of envelope (bottom).

observed and calculated seismograms for the surface time window. The correlation coefficient for first, second and third moments are 0.91, 0.89, 0.37. Figure 5.14 shows the correlation of first, second and third moment between observed seismograms for tangential components. The correlation coefficients are -0.51, 0.19 and 0.42 respectively. The correlations are quite poor. We will, however, perform further analysis of the tangential component.

The parameterizations that have a correlation coefficient 0.7 or higher are used in the source mechanism studies. These parameterizations will be tested further in the next chapter to understand their sensitivity to different source mechanisms.



Moments of P waves envelopes

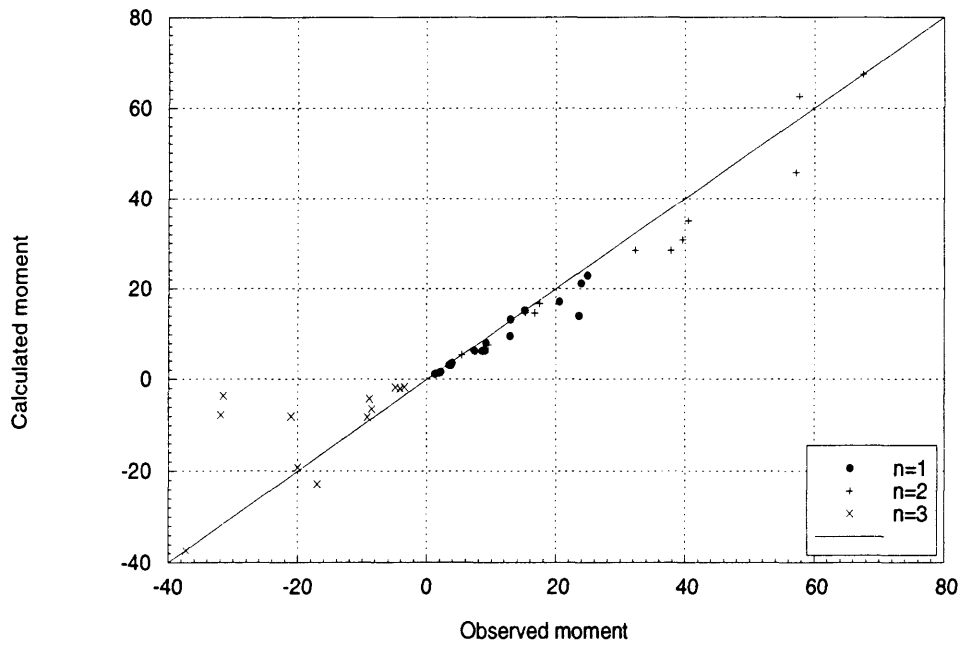


Figure 5.12: Selected observed (first row) and calculated seismograms (second row) for the *P*-wave time window and the correlation between the moments of the envelopes of the observed and calculated seismograms. M is the total moment.

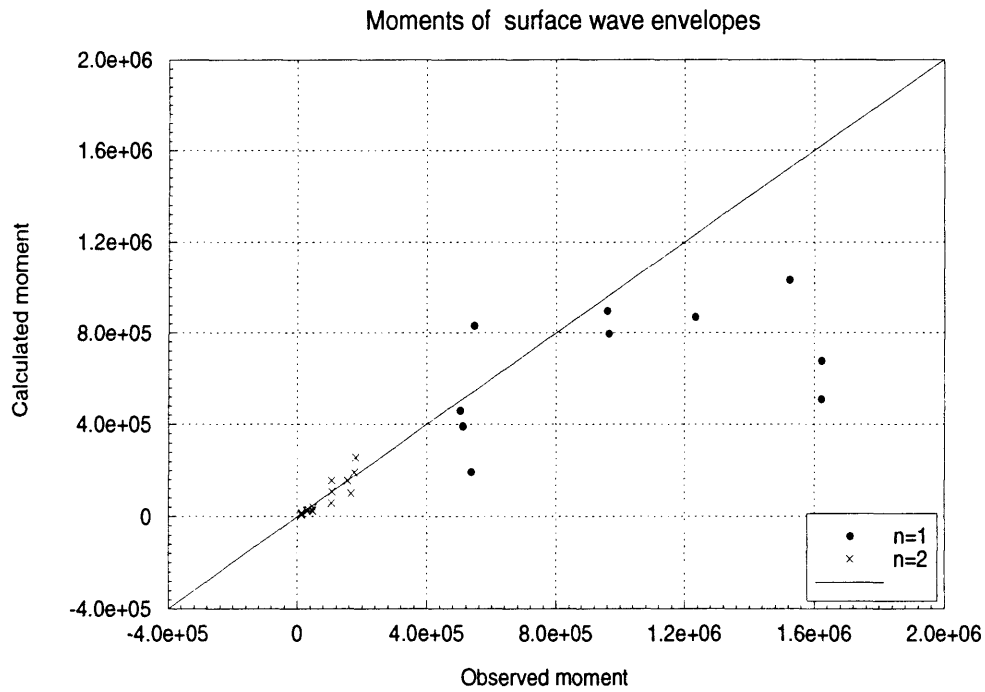
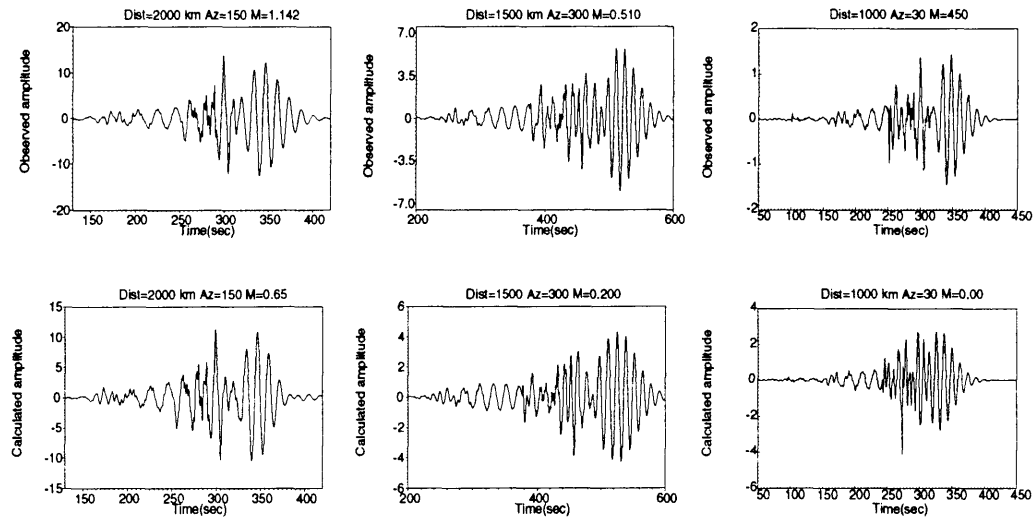


Figure 5.13: Selected observed(first row) and calculated seismograms(second row) for the surface time window and the correlation between the moments of the envelopes of the observed seismograms and calculated seismograms. M is the total moment.

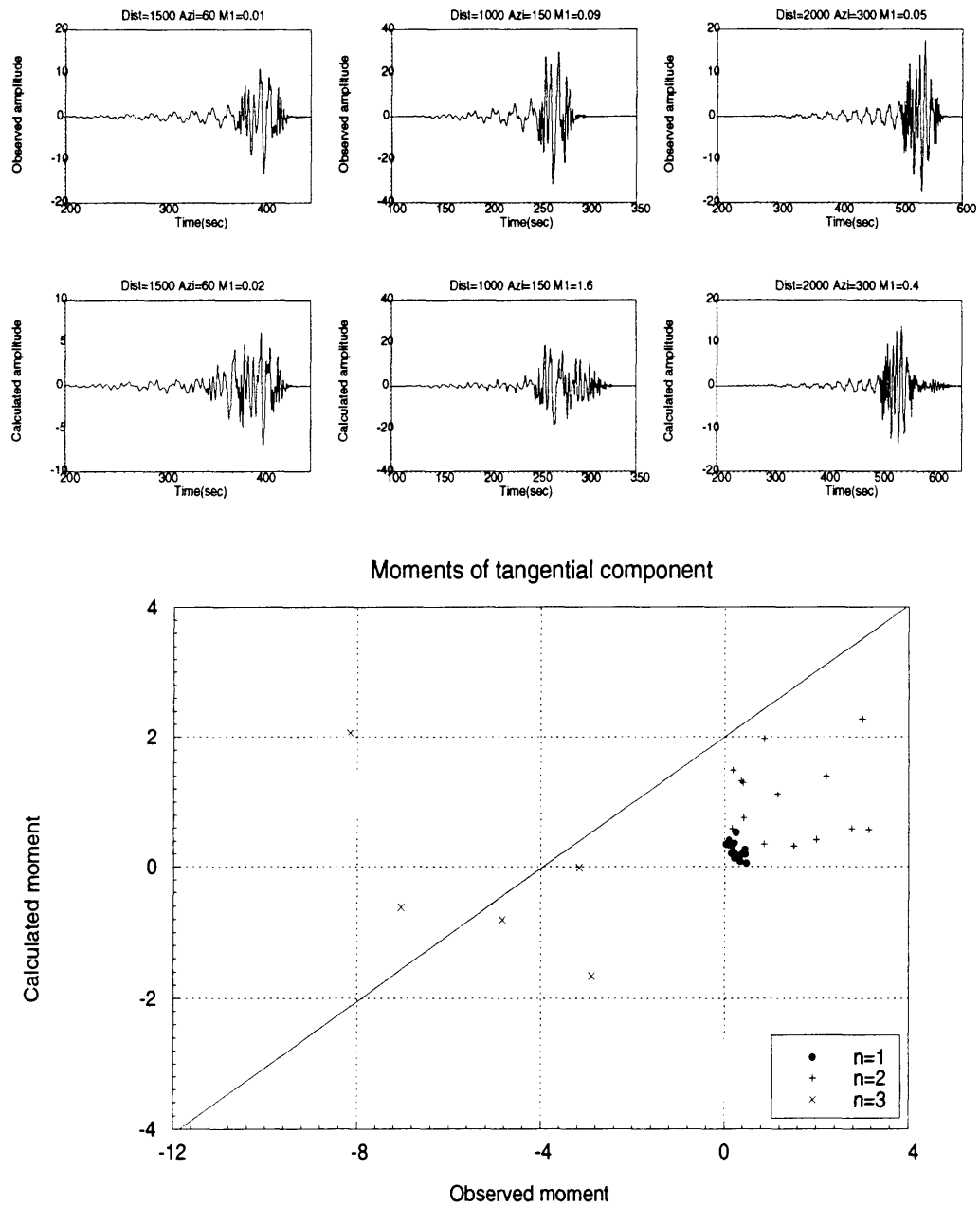


Figure 5.14: Selected observed (first row) and calculated seismograms (second row) for the tangential component and the correlation between the moments of the envelopes of the observed and calculated seismograms. M is the total moment

5.4 Grid Search

During the last two decades, the inversion of geophysical observations has become one of the most important tools in the evaluation of geophysical data. These techniques, however, have several disadvantages. The solution usually depends on data quality, the formulation of the forward problem, the initial guess and constraints, and integration with other observations. Most of the time, therefore, the interpreter must eliminate solutions by including a priori constraints. Some of the principal goals of this study are to understand, the nature of the solution space, identify local minima, and understand how to construct confidence limits about a final solution.

To begin to quantify these objectives, we explore the error surfaces of the parameterizations described in the previous section by performing a grid search on the source parameters. The grid search is performed with a 10° spacing over ranges, $0^\circ < \delta < 90^\circ$, $0^\circ < \lambda < 180^\circ$ and $0^\circ < \phi < 180^\circ$. Since the fundamental Green's functions are calculated for a unit seismic moment, we scale the seismograms to remove the effect of seismic moment.

The grid search and scaling are performed in two steps. First, the higher order moments are scaled by the zeroth moment (area) of the seismogram's envelope at every grid point since higher order moments of the envelopes depend on the shape of the envelopes more than amplitudes of the envelopes. It is, however, important to include zeroth moment (area) in the grid search since it contains information on the

source parameters. The seismic moment is estimated from the best solution after the grid search using the ratio:

$$M_0 = \frac{\mu_0^o}{\mu_0^c} \quad (5.5)$$

where μ_0^o is the zeroth moment of observed seismograms and μ_0^c is the zeroth moment of the calculated seismogram for the best solution after the grid search. In the second step, seismograms are scaled by the estimated seismic moment and the grid search is performed again. The scaling is applied to all parameterizations, area, energy, and moments.

The-Root-Mean-Square (RMS) error is used to evaluate the misfit between area, energy, and statistical moments of the envelopes of the observed seismograms and those of the synthetic seismograms. The results of the grid search can be interpreted individually for different parameterizations, or can be combined together so that possible local minima are eliminated or that a deeper global minimum is obtained. Since different moments have different units, they are scaled as

$$\mu_{total} = \frac{\int_{t_0}^{t_1} (t - \mu) f(t) dt}{\int_{t_0}^t t dt} + \frac{\int_{t_0}^{t_1} (t - \mu)^2 f(t) dt}{\int_{t_0}^{t_1} t^2 dt} + \frac{\int_{t_0}^{t_1} (t - \mu)^3 f(t) dt}{\int_{t_0}^{t_1} t^3 dt} \quad (5.6)$$

when combining them into a single RMS estimate.

Before systematically exploring the parameterizations described in the previous chapter, consider observations generated from a source with $\phi_s = 30^\circ$, $\delta = 60^\circ$, $\lambda = 60^\circ$. Figure 5.15 shows RMS error surface calculated from a grid search of the solution space using equation (5.6) and the first 3 statistical moments of the P waveforms.

Some of the waveforms used for the calculation are displayed on the top and the station distribution is shown on a circle. 15 stations are used in the calculations. Dark areas indicate where the RMS error becomes minimum. Since plots are saturated at 0.07, the minimum on the surface cannot be observed. The large dark area seen on the top of the block is a continuation of two minima observed in the block. The first one is close to the true solution at $\phi_s = 30^\circ, \delta = 40^\circ, \lambda = 50^\circ$ (Figure 5.16) and the second one is $\phi_s = 80^\circ, \delta = 50^\circ, \lambda = 130^\circ$ (Figure 5.17). The ratio of maximum and minimum RMS values for these solutions is not considerably different. It is, however, interesting to note that the solution, $\phi_s = 80^\circ, \delta = 50^\circ, \lambda = 130^\circ$, is not related to the true solution or its conjugate. Similar solutions are found during the grid search for different source mechanisms and they will be evaluated later in this chapter.

As another example, Figure (5.18) shows RMS error surface for the source mechanism, $\phi_s = 0^\circ, \delta = 90^\circ, \lambda = 0^\circ$. This example is particularly important since several minima are observed after the grid search. All of them are, however, represent the same solution with the exception of polarities. Polarity information of *P-waves* will help to eliminate some of these solutions.

Next, consider the tangential component of the wavefield. The tangential component cannot be used alone for source mechanism studies since *SH-waves* are not dependent on the m_6 component of the moment tensor, and there is a linear dependence between m_1 and m_3 (Koch, 1991). Therefore, it is not possible to resolve all

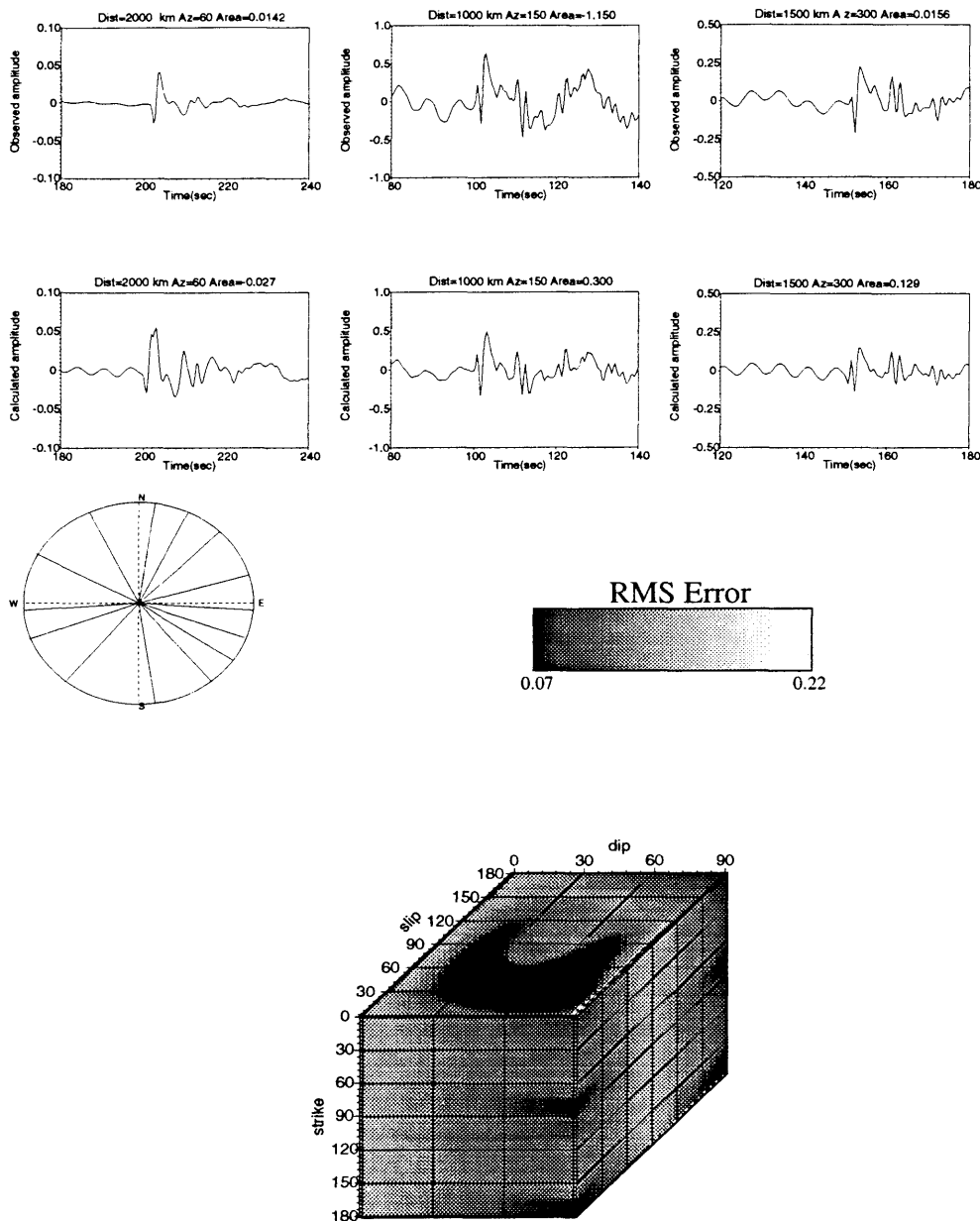


Figure 5.15: RMS error surface using the first three statistical moments of the *P*-wave envelope. A source mechanism of $\phi_s = 30^\circ, \delta = 60^\circ, \lambda = 60^\circ$ is used to generate the observed seismograms. The lower right-hand portion of the figure shows the error surface from a grid search of the solution space. The circle to the left shows the azimuthal distribution of observations, and several examples of the observed and computed waveforms are generated from the best solution found in the grid search. Plot saturation occurs at misfits of 0.07 and 0.22. The actual misfits range between 0.05 and 0.24.

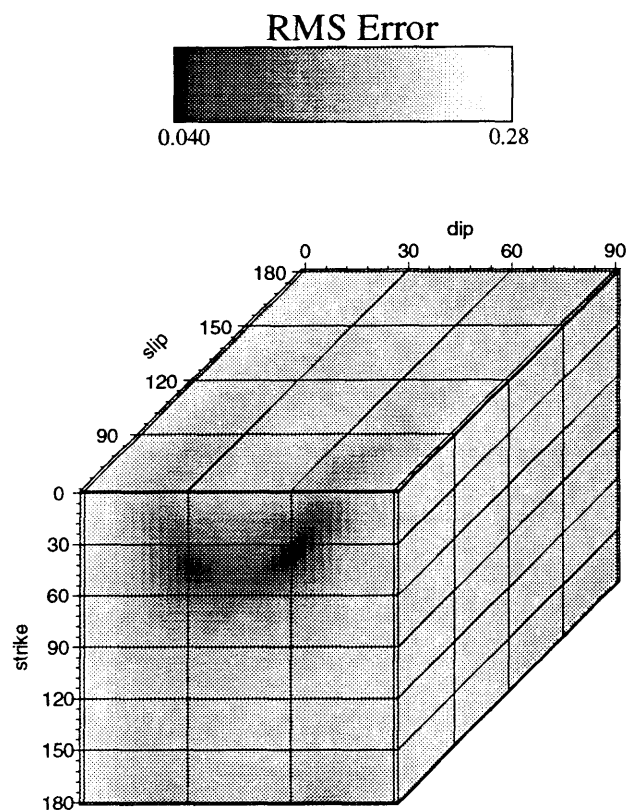


Figure 5.16: A slice through the error surface at $\lambda = 60^\circ$ in Figure. Plot saturation occurs at misfits of 0.04 and 0.28. The actual misfits range between 0.035 and 0.30.

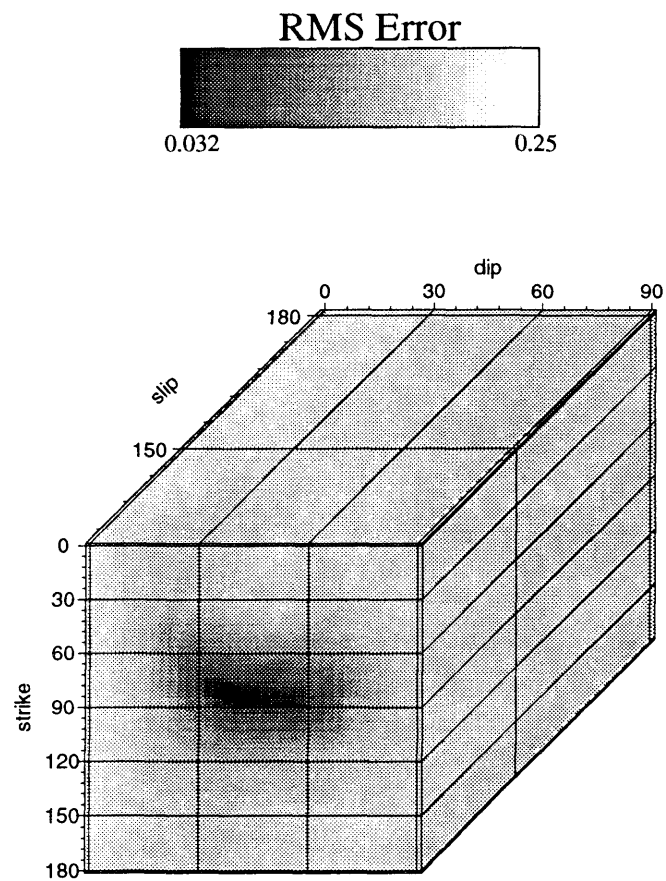


Figure 5.17: A slice through the error surface shown in Figure at $\lambda = 130^\circ$. Plot saturation occurs at misfits of 0.032 and 0.25. The actual misfits range from between 0.032 and 0.27.

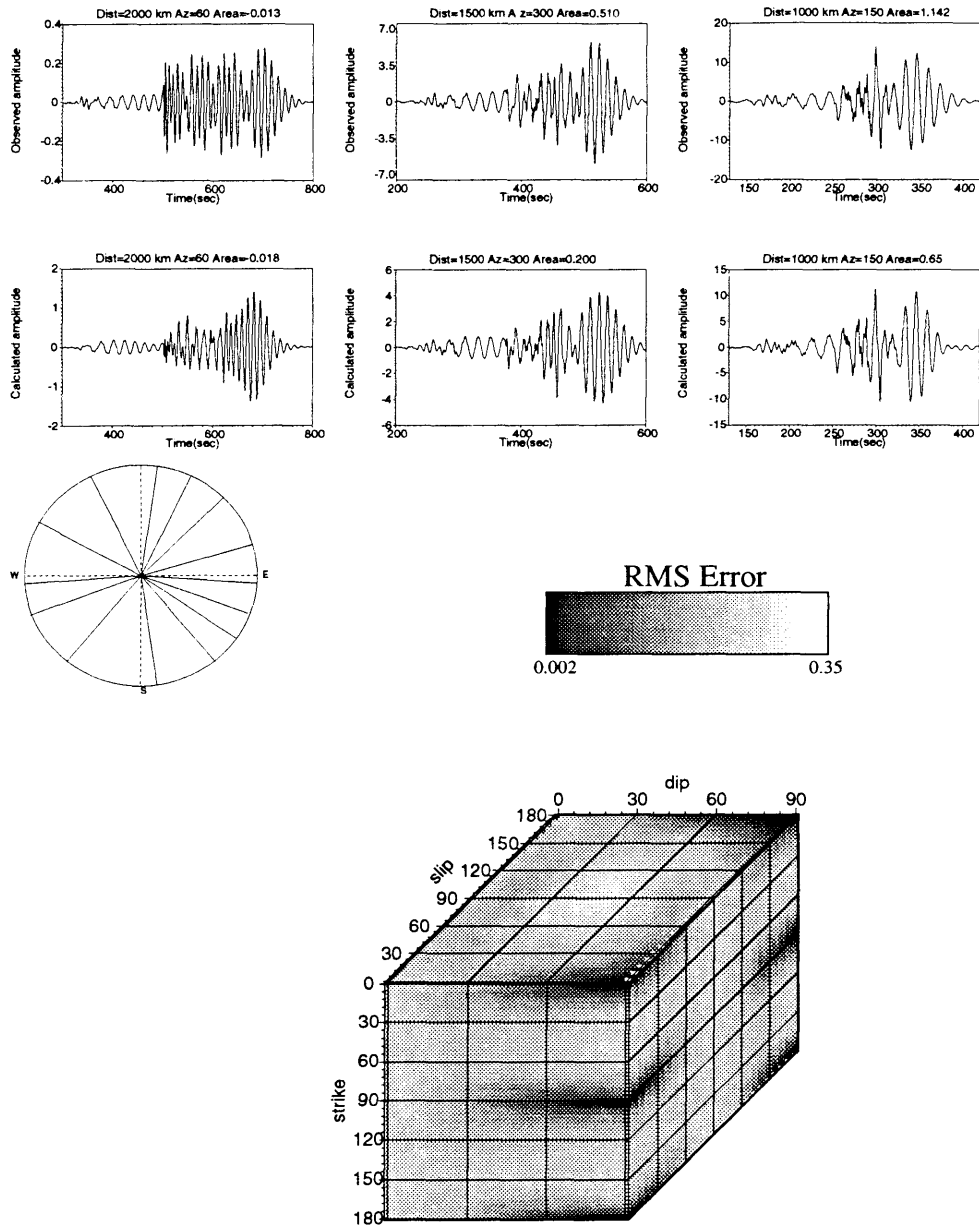


Figure 5.18: RMS error surface using the first three statistical moments of the *Surface waves* envelope. A source mechanism of $\phi_s = 0^\circ$, $\delta = 90^\circ$, $\lambda = 0^\circ$ is used to generate the observed seismograms. The lower right-hand portion of the figure shows the error surface from a grid search of the solution space. The circle to the left shows the azimuthal distribution of observations, and several examples of the observed and computed waveforms are generated from the best solution found in the grid search. Plot saturation occurs at misfits of 0.22 and 0.35. The actual misfits range from between 0.07 and 0.44.

of the components of the seismic moment tensor from the tangential component. We can, however, combine the tangential component with radial and vertical component data. The results of the grid search using tangential component alone are shown in Figure (5.19) for the source mechanism, $\phi_s = 30^\circ, \delta = 60^\circ, \lambda = 60^\circ$. Significantly more minima occur on the grid surface than when using vertical component observations. Figure (5.20) shows a profile taken at $\lambda = 60^\circ$ where the global minimum is expected at $\phi_s = 30^\circ, \delta = 60^\circ, \lambda = 60^\circ$ but the the global minimum is observed at $\phi_s = 100^\circ, \delta = 30^\circ, \lambda = 60^\circ$. The main reason for this unsatisfactory result is that the shape of the *SH* seismograms at these regional distances does not change sufficiently for different source mechanisms. Therefore, combining this data set with vertical component data is not expected to help further to constraint source parameters. Since the tangential component shows such a poor resolution it will not be considered further.

Parameterizations described in the previous section which have correlation coefficients greater than 0.7 are tested for 50 different source mechanisms to understand their sensitivity to source mechanism. Although the area of *P-waves* has a large correlation coefficient, the grid search for this parameterization is not successful. The results are displayed in Tables 5.1-5.4. Tables 5.1 and 5.2 are calculated using waveform energy and Tables 5.3 and 5.4 are calculated using the statistical moments of the envelopes of *P-waves* and surface waves. Multiple solutions, with

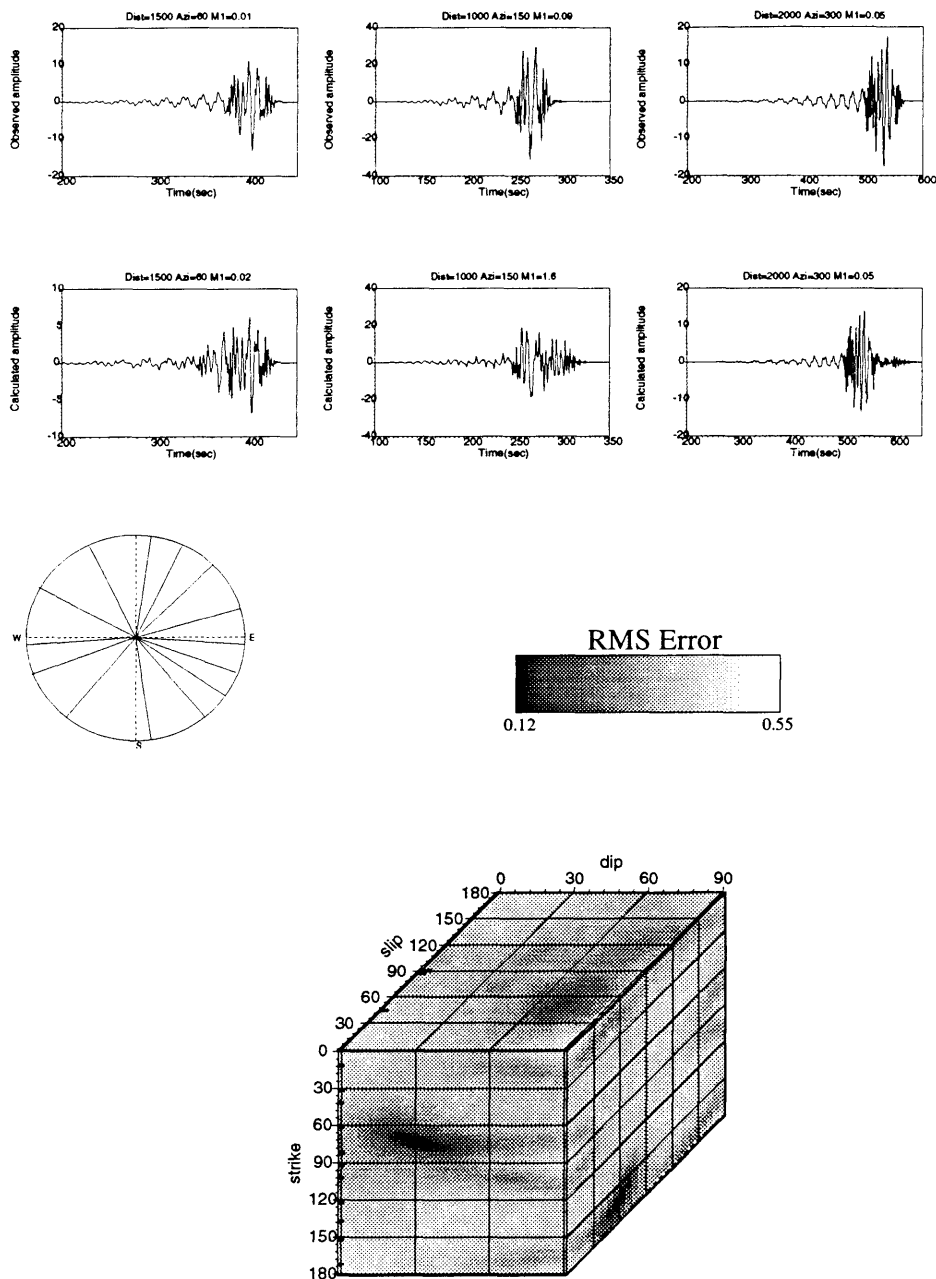


Figure 5.19: RMS error surface using the first 3 statistical moments of the tangential component. A source mechanism of $\phi_s = 30^\circ, \delta = 60^\circ, \lambda = 60^\circ$ is used to generate the observed seismograms. The lower right-hand portion of the figure shows the error surface from a grid search of the solution space. The circle to the left shows the azimuthal distribution of observations, and several examples of the observed and computed waveforms are generated from the best solution found in the grid search. Plot saturation occurs at misfits of 0.12 and 0.55. The actual misfits range from between 0.12 and 0.55.

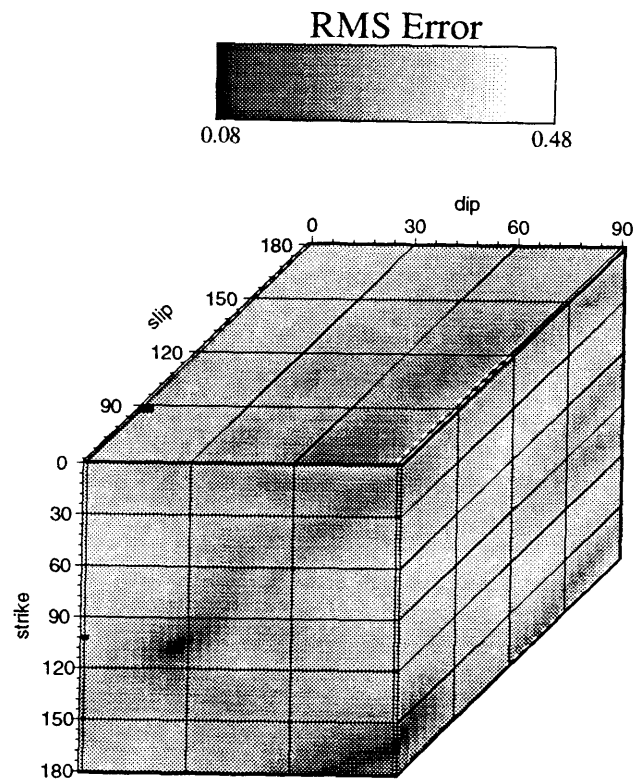


Figure 5.20: A slice through the error surface at $\lambda = 60^\circ$ in Figure . Plot saturation occurs at misfits of 0.08 and 0.48. The actual misfits range from between 0.0 and 0.55.

similar RMS errors, are found for most of these 50 source mechanisms. Some of the solutions represent conjugate nodal planes. Question marks indicate source mechanisms that are not constrained by the grid search. The principal reason for having such unconstrained solutions is that one or some of the moment tensor components for these source types are zero. As an example, consider the source mechanism with $\phi_s = 60^\circ, \delta = 90^\circ, \lambda = 90^\circ$. Table (5.5) shows the moment tensor for this source mechanism. The only contribution comes from the dip slip component of the fundamental Green's function.

Table 5.1: Source mechanism solutions after the grid search from *P*-wave energy.

Trial	True Sol [†]	Aux Plane	Max RMS	1		2		3	
				Solution	RMS	Solution	RMS	Solution	RMS
1	0/0/30	240/90/90	?	?	?	?	?	?	?
2	0/0/60	210/90/90	?	?	?	?	?	?	?
3	0/0/90	180/90/90	?	?	?	?	?	?	?
4	0/30/0	270/90/120	0.21	0/30/0	0.0094	0/90/60	0.0096	90/90/120	0.001
5	0/30/30	243/76/117	0.20	0/30/30	0.016	60/30/140	0.017	-	-
6	0/30/60	213/64/106	0.22	30/60/110	0.028	10/30/80	0.029	-	-
7	0/30/90	180/60/90	0.24	170/50/80	0.031	10/40/110	0.031	-	-
8	0/60/0	270/90/150	0.17	0/80/0	0.019	90/90/0	0.020	180/90/180	0.020
9	0/60/30	253/64/146	0.25	0/50/60	0.032	40/40/120	0.035	-	-
10	0/60/60	224/41/131	0.25	0/50/60	0.033	40/40/120	0.035	-	-
11	0/60/90	180/30/90	0.27	0/40/90	0.032	170/40/80	0.034	-	-
12	0/90/0	270/90/180	0.19	0/90/0	0.039	180/90/0	0.040	90/90/180	0.042
13	0/90/30	270/60/180	0.17	0/80/170	0.018	90/80/0	0.020	180/90/180	0.020
14	0/90/60	270/30/180	0.19	180/30/180	0.010	90/90/120	0.011	0/90/60	0.012
15	0/90/90	0/0/90	?	?	?	?	?	?	?
16	30/30/0	300/90/120	0.20	120/90/120	0.008	30/90/60	0.009	30/30/0	0.010
17	30/30/30	23/76/117	0.23	30/30/30	0.015	90/30/150	0.017	-	-
18	30/30/60	244/64/116	0.24	60/30/110	0.029	40/30/60	0.031	60/60/110	0.034
19	30/30/90	210/60/90	0.24	40/40/110	0.035	30/40/90	0.038	-	-
20	30/60/0	300/90/150	0.17	120/90/170	0.017	30/90/0	0.018	30/70/0	0.02
21	30/60/30	283/64/146	0.25	30/60/30	0.027	100/60/150	0.03	-	-
22	30/60/60	254/41/131	0.28	80/50/130	0.032	30/50/50	0.035	-	-
23	30/60/90	210/30/90	0.25	40/40/110	0.034	30/40/90	0.037	-	-
24	30/90/0	300/90/180	0.19	30/90/0	0.038	120/90/0	0.038	120/90/180	0.038
25	30/90/30	300/60/180	0.17	120/90/170	0.017	30/90/10	0.018	120/90/0	0.020

[†] strike/dip/slip in degrees using the convention of Aki and Richards (1980).

Table 5.1 continued

Trial	True Sol	Aux Plane	Max RMS	1		2		3	
				Solution	RMS	Solution	RMS	Solution	RMS
26	30/90/60	300/30/180	0.19	120/90/120	0.09	30/90/60	0.10	30/30/0	0.11
27	30/90/90	300/0/90	?	?	?	?	?	?	?
28	60/30/0	330/90/120	0.20	60/30/0	0.07	150/90/60	0.9	60/30/180	0.10
29	60/30/30	303/76/117	0.22	60/30/30	0.013	120/30/150	0.016	-	-
30	60/30/60	273/64/106	0.24	90/30/110	0.026	60/60/70	0.028	60/30/60	0.029
31	60/30/90	240/60/90	0.25	60/60/90	0.039	60/30/90	0.040	-	-
32	60/60/0	330/90/150	0.18	150/90/160	0.015	60/90/10	0.016	150/90/10	0.018
33	60/60/30	313/64/146	0.25	60/60/30	0.021	140/60/150	0.026	-	-
34	60/60/60	289/41/130							
35	60/60/90	240/30/90	0.25	60/60/90	0.039	70/40/110	0.040	-	-
36	60/90/0	330/90/180	0.16	60/90/0	0.024	150/90/0	0.024	150/90/180	0.024
37	60/90/30	330/60/180	0.17	60/90/20	0.016	150/90/20	0.017	60/80/180	0.017
38	60/90/60	330/30/180	0.20	60/90/60	0.007	150/90/60	0.008	60/30/0	0.008
39	60/90/90	285/0/135	?	?	?	?	?	?	?
40	90/30/0	360/90/120	0.33	180/90/0	0.017	90/90/60	0.019	90/30/180	0.020
41	90/30/30	333/75/116	0.23	90/40/30	0.014	160/40/150	0.015	150/70/120	0.016
42	90/30/60	303/64/106	0.25	90/60/70	0.023	100/30/70	0.026	120/30/110	0.028
43	90/30/90	270/60/90	0.24	80/40/70	0.034	100/60/100	0.035	-	-
44	90/60/0	360/90/150	0.17	0/80/170	0.018	90/80/0	0.019	180/80/170	0.020
45	90/60/30	343/64/146	0.27	90/60/30	0.033	160/60/140	0.035	-	-
46	90/60/60	319/41/130	0.30	100/50/60	0.029	140/50/120	0.030	-	-
47	90/60/90	270/30/90	0.24	80/40/70	0.035	100/50/100		-	-
48	90/90/0	360/90/180	0.24	90/90/0	0.039	180/90/0	0.039	0/90/0	0.039
49	90/90/30	360/60/180	0.23	90/90/0	0.018	90/90/180	0.018	180/90/180	0.018
50	90/90/60	360/30/180	0.19	0/40/180	0.013	90/90/120	0.015	90/90/50	0.016

Table 5.2: Source mechanism solutions after the grid search from surface wave energy.

Trial	True Sol†	Aux Plane	Max RMS	1		2		3	
				Solution	RMS	Solution	RMS	Solution	RMS
1	0/0/30	240/90/90	?	?	?	?	?	?	?
2	0/0/60	210/90/90	?	?	?	?	?	?	?
3	0/0/90	180/90/90	?	?	?	?	?	?	?
4	0/30/0	270/90/120	0.73	180/30/0	0.018	90/90/120	0.018	180/30/180	0.018
5	0/30/30	243/76/117	0.72	10/20/50	0.026	180/30/30	0.031	60/20/130	0.036
6	0/30/60	213/64/106	0.66	40/30/130	0.052	170/30/50	0.060	0/30/60	0.072
7	0/30/90	180/60/90	0.65	10/30/110	0.067	170/30/70	-	-	-
8	0/60/0	270/90/150	0.65	0/50/0	0.029	90/50/0	0.030	90/90/140	0.031
9	0/60/30	253/64/146	0.81	40/70/0	0.035	70/40/150	0.041	180/70/40	0.042
10	0/60/60	224/41/131	0.75	50/40/140	0.050	170/60/40	0.067	-	-
11	0/60/90	160/50/70	0.65	10/30/110	0.068	170/30/70	0.079	-	-
12	0/90/0	270/90/180	0.64	0/90/20	0.037	90/90/180	0.038	180/90/180	0.039
13	0/90/30	90/80/30	0.65	90/50/0	0.029	180/90/40	0.029	0/90/140	0.031
14	0/90/60	270/30/180	0.72	0/90/60	0.021	180/30/0	0.023	90/90/120	0.025
15	0/90/90	0/0/90	?	?	?	?	?	?	?
16	30/30/0	300/90/120	0.73	30/30/0	0.019	120/90/60	0.019	120/90/120	0.023
17	30/30/30	23/76/117	0.81	100/30/150	0.028	30/30/30	0.037	-	-
18	30/30/60	244/64/116	0.83	70/30/130	0.056	30/30/60	0.061	-	-
19	30/30/90	210/60/90	0.74	10/30/60	0.062	40/30/110	0.065	-	-
20	30/60/0	300/90/150	0.64	30/60/0	0.047	30/90/30	0.048	120/90/150	0.040
21	30/60/30	283/64/146	0.86	30/70/40	0.035	110/60/150	0.055	-	-
22	30/60/60	254/41/131	0.91	40/30/60	0.050	80/40/140	0.062	30/60/50	0.066
23	30/60/90	210/30/90	0.75	10/30/60	0.064	40/30/110	0.065	-	-
24	30/90/0	300/90/180	0.60	30/90/20	0.048	120/90/20	0.051	30/70/180	0.051
25	30/90/30	300/60/180	0.64	30/90/30	0.044	120/60/0	0.048	120/90/150	0.050

† strike/dip/slip in degrees using the convention of Aki and Richards (1980).

Table 5.2 continued

Trial	True Sol	Aux Plane	Max RMS	1		2		3	
				Solution	RMS	Solution	RMS	Solution	RMS
26	30/90/60	300/30/180	0.73	30/90/60	0.017	30/30/0	0.023	120/90/60	0.023
27	30/90/90	300/0/90	?	?	?	?	?	?	?
28	60/30/0	330/90/120	0.74	60/30/0	0.013	150/90/60	0.013	60/30/180	0.013
29	60/30/30	303/76/117	0.78	60/30/30	0.020	130/30/150	0.035	-	-
30	60/30/60	273/64/106	0.83	100/30/130	0.044	60/30/60	0.054	-	-
31	60/30/90	240/60/90	0.84	50/30/70	0.064	80/30/120	0.067	-	-
32	60/60/0	330/90/150	0.65	60/60/0	0.026	150/90/30	0.027	60/90/150	0.029
33	60/60/30	313/64/146	0.80	60/60/30	0.024	-	-	-	-
34	60/60/60	289/41/130	0.85	60/60/60	0.05	110/60/120	0.057	-	-
35	60/60/90	240/30/90	0.84	50/30/70	0.062	80/30/120	0.066	60/60/90	0.074
36	60/90/0	330/90/180	0.61	150/70/0	0.030	60/70/0	0.031	-	-
37	60/90/30	330/60/180	0.65	60/90/150	0.027	150/60/0	0.027	150/90/30	0.027
38	60/90/60	330/30/180	0.74	150/30/0	0.011	60/90/120	0.011	60/90/60	0.017
39	60/90/90	285/0/135	0.61	150/70/0	0.030	60/70/0	0.031	150/90/180	0.031
40	90/30/0	360/90/120	0.72	180/30/0	0.022	0/90/60	0.022	90/90/120	0.02
41	90/30/30	333/75/116	0.75	150/30/150	0.028	90/30/30	0.031	-	-
42	90/30/60	303/64/106	0.80	130/30/130	0.051	80/30/50	0.053	-	-
43	90/30/90	270/60/90	0.78	80/30/70	0.050	100/60/100	0.060	-	-
44	90/60/0	360/90/150	0.65	90/50/0	0.029	90/90/40	0.031	90/90/140	0.036
45	90/60/30	343/64/146	0.79	90/70/40	0.042	160/70/140	0.045	-	-
46	90/60/60	319/41/130	0.85	80/50/40	0.048	140/40/130	0.055	-	-
47	90/60/90	270/30/90	0.78	80/30/70	0.049	80/60/80	0.058	-	-
48	90/90/0	360/90/180	?	?	?	?	?	?	?
49	90/90/30	360/60/180	0.65	90/90/40	0.029	90/90/140	0.030	90/50/180	0.036
50	90/90/60	360/30/180	0.67	180/30/0	0.017	90/90/120	0.017	180/30/180	0.017

Table 5.3: Source mechanism solutions after the grid search from the moments of *P*-wave envelope.

Trial	True Sol [†]	Aux Plane	Max RMS	1		2		3	
				Solution	RMS	Solution	RMS	Solution	RMS
1	0/0/30	240/90/90	?	?	?	?	?	?	?
2	0/0/60	210/90/90	?	?	?	?	?	?	?
3	0/0/90	180/90/90	?	?	?	?	?	?	?
4	0/30/0	270/90/120	0.19	0/40/0	0.013	0/90/50	0.014	90/90/130	0.015
5	0/30/30	243/76/117	0.23	0/40/30	0.021	60/30/50	0.024	-	-
6	0/30/60	213/64/106	0.27	10/40/60	0.024	30/60/110	0.026	-	-
7	0/30/90	180/60/90	0.32	0/50/90	0.023	-	-	-	-
8	0/60/0	270/90/150	0.21	0/80/0	0.018	0/80/180	0.019	90/90/10	0.019
9	0/60/30	253/64/146	0.25	0/60/30	0.033	180/60/30	0.034	-	-
10	0/60/60	224/41/131	0.28	0/50/60	0.032	40/40/120	0.033	-	-
11	0/60/90	180/30/90	0.32	0/50/90	0.024	180/50/90	0.025	-	-
12	0/90/0	270/90/180	0.24	0/90/0	0.039	90/90/180	0.040	180/90/0	0.042
13	0/90/30	270/60/180	0.21	0/90/10	0.018	90/90/20	0.019	0/90/180	0.020
14	0/90/60	270/30/180	0.19	0/90/130	0.012	0/40/90	0.013	90/90/50	0.014
15	0/90/90	0/0/90	?	?	?	?	?	?	?
16	30/30/0	300/90/120	0.20	30/40/0	0.14	120/90/50	0.015	120/40/0	0.016
17	30/30/30	23/76/117	0.26	30/30/30	0.021	90/30/150	0.026	-	-
18	30/30/60	244/64/116	0.25	30/40/60	0.028	40/60/80	0.030	60/60/110	0.032
19	30/30/90	210/60/90	0.30	20/50/80	0.027	30/50/90	0.028	-	-
20	30/60/0	300/90/150	0.21	30/80/0	0.016	120/80/0	0.016	30/80/180	0.017
21	30/60/30	283/64/146	0.25	30/60/30	0.031	-	-	-	-
22	30/60/60	254/41/131	0.28	30/40/50	0.033	80/60/120	0.037	-	-
23	30/60/90	210/30/90	0.30	20/40/80	0.029	30/40/100	0.033	-	-
24	30/90/0	300/90/180	0.25	30/90/0	0.037	120/90/0	0.037	30/90/180	0.037
25	30/90/30	300/60/180	0.21	120/80/0	0.016	30/90/170	0.016	-	-

[†] strike/dip/slip in degrees using the convention of Aki and Richards (1980).

Table 5.3 continued

Trial	True Sol	Aux Plane	Max RMS	1		2		3	
				Solution	RMS	Solution	RMS	Solution	RMS
26	30/90/60	300/30/180	0.20	120/40/0	0.013	30/90/130	0.014	120/90/130	0.014
27	30/90/90	300/0/90	?	?	?	?	?	?	?
28	60/30/0	330/90/120	0.20	60/90/50	0.013	150/90/130	0.014	-	-
29	60/30/30	303/76/117	0.24	60/40/30	0.021	120/30/150	0.024	-	-
30	60/30/60	273/64/106	0.23	60/40/60	0.026	90/60/100	0.029	90/60/100	0.029
31	60/30/90	240/60/90	0.26	60/40/90	0.029	70/50/100	0.032	-	-
32	60/60/0	330/90/150	0.20	60/90/0	0.016	150/90/0	0.016	-	-
33	60/60/30	313/64/146	0.25	60/60/30	0.028	-	-	-	-
34	60/60/60	289/41/130	0.26	60/60/60	0.033	110/60/120	0.035	-	-
35	60/60/90	240/30/90	0.27	60/50/90	0.029	-	-	-	-
36	60/90/0	330/90/180	0.23	60/90/0	0.033	150/90/0	0.033	-	-
37	60/90/30	330/60/180	0.20	60/80/0	0.017	150/90/0	0.017	60/90/180	0.017
38	60/90/60	330/30/180	0.20	60/90/50	0.014	150/90/130	0.017	60/90/130	0.018
39	60/90/90	285/0/135	?	?	?	?	?	?	?
40	90/30/0	360/90/120	0.19	90/40/0	0.013	180/90/50	0.013	0/90/130	0.013
41	90/30/30	333/75/116	0.25	90/40/30	0.019	160/40/150	0.023	-	-
42	90/30/60	303/64/106	0.24	90/40/60	0.025	130/50/120	0.029	-	-
43	90/30/90	270/60/90	0.25	90/50/90	0.029	-	-	-	-
44	90/60/0	360/90/150	0.21	90/90/0	0.019	180/90/0	0.019	180/90/180	0.019
45	90/60/30	343/64/146	0.26	90/60/30	0.036	-	-	-	-
46	90/60/60	319/41/130	0.28	90/50/50	0.038	140/40/130	0.037	-	-
47	90/60/90	270/30/90	0.27	90/50/90	0.029	0/40/90	-	-	-
48	90/90/0	360/90/180	0.24	90/90/0	0.039	180/90/0	0.039	0/90/0	0.039
49	90/90/30	360/60/180	0.23	90/90/0	0.018	90/90/180	0.018	180/90/180	0.018
50	90/90/60	360/30/180	0.19	0/40/180	0.013	90/90/120	0.015	90/90/50	0.016

Table 5.4: Source mechanism solutions after the grid search from the moments of surface wave envelope.

Trial	True Sol [†]	Aux Plane	Max RMS	1		2		3	
				Solution	RMS	Solution	RMS	Solution	RMS
1	0/0/30	240/90/90	?	?	?	?	?	?	?
2	0/0/60	210/90/90	?	?	?	?	?	?	?
3	0/0/90	180/90/90	?	?	?	?	?	?	?
4	0/30/0	270/90/120	0.81	0/40/0	0.16	0/90/50	0.21	-	-
5	0/30/30	243/76/117	0.61	0/30/0	0.10	60/90/90	0.10	90/90/120	0.11
6	0/30/60	213/64/106	0.71	170/60/170	0.17	30/40/130	0.18	10/30/80	0.19
7	0/30/90	180/60/90	0.84	160/50/70	0.21	10/50/100	0.23	-	-
8	0/60/0	270/90/150	0.87	0/80/0	0.14	0/80/180	0.22	90/90/10	0.24
9	0/60/30	253/64/146	0.66	0/50/20	0.16	70/70/140	0.17	-	-
10	0/60/60	224/41/131	0.78	10/50/50	0.17	40/50/130	0.19	-	-
11	0/60/90	160/50/70	0.85	10/50/100	0.16	160/50/70	0.18	-	-
12	0/90/0	270/90/180	0.67	0/90/0	0.19	90/90/0	0.19	90/90/90	0.19
13	0/90/30	90/80/30	0.74	180/80/160	0.16	0/80/170	0.19	-	-
14	0/90/60	270/30/180	0.63	0/90/60	0.10	180/90/120	0.10	90/30/180	0.12
15	0/90/90	0/0/90	?	?	?	?	?	?	?
16	30/30/0	300/90/120	0.60	30/30/0	0.09	120/90/120	0.08	-	-
17	30/30/30	23/76/117	0.67	30/30/30	0.11	100/30/150	0.11	90/80/110	0.12
18	30/30/60	244/64/116	0.64	40/20/90	0.17	30/30/70	0.18	-	-
19	30/30/90	210/60/90	0.78	20/50/80	0.19	30/60/90	0.21	-	-
20	30/60/0	300/90/150	0.63	120/80/10	0.15	30/70/10	0.17	-	-
21	30/60/30	283/64/146	0.67	30/50/20	0.14	110/70/150	0.19	-	-
22	30/60/60	254/41/131	0.73	40/30/60	0.15	70/30/120	0.17	-	-
23	30/60/90	210/30/90	0.78	10/30/80	0.19	30/40/110	0.20	-	-
24	30/90/0	300/90/180	0.68	120/80/10	0.19	30/90/0	0.21	-	-
25	30/90/30	300/60/180	0.62	120/80/20	0.15	30/80/10	0.16	-	-

[†] strike/dip/slip in degrees using the convention of Aki and Richards (1980).

Table 5.4 continued

Trial	True Sol	Aux Plane	Max RMS	1		2		3	
				Solution	RMS	Solution	RMS	Solution	RMS
26	30/90/60	300/30/180	0.58	10/90/60	0.09	120/90/120	0.10	-	-
27	30/90/90	300/0/90	?	?	?	?	?	?	?
28	60/30/0	330/90/120	0.62	150/90/120	0.08	60/30/0	0.08	150/90/60	0.09
29	60/30/30	303/76/117	0.74	130/30/150	0.07	70/30/70	0.09	-	-
30	60/30/60	273/64/106	0.65	70/30/60	0.13	100/30/120	0.15	-	-
31	60/30/90	240/60/90	0.68	60/60/90	0.19	60/30/80	0.20	-	-
32	60/60/0	330/90/150	0.60	60/70/0	0.19	150/90/0	0.20	150/90/150	0.21
33	60/60/30	313/64/146	0.75	60/60/30	0.12	140/60/150	0.14	-	-
34	60/60/60	289/41/130	0.72	70/60/50	0.13	110/40/130	0.14	-	-
35	60/60/90	240/30/90	0.68	60/60/90	0.19	70/30/100	0.19	-	-
36	60/90/0	330/90/180	0.65	60/90/0	0.17	150/90/0	0.18	-	-
37	60/90/30	330/60/180	0.59	60/90/20	0.14	150/90/150	0.15	-	-
38	60/90/60	330/30/180	0.62	60/90/60	0.08	60/90/120	0.09	-	-
39	60/90/90	195/0/45	?	?	?	?	?	?	?
40	90/30/0	0/90/120	0.64	100/30/10	0.10	0/90/60	0.11	0/90/120	0.12
41	90/30/30	333/90/116	0.81	90/40/30	0.09	160/40/150	0.09	-	-
42	90/30/60	303/64/106	0.76	130/60/110	0.11	100/60/70	0.12	-	-
43	90/30/90	303/64/106	0.65	100/30/90	0.13	110/60/100	0.14	-	-
44	90/60/0	270/60/90	0.60	90/70/10	0.15	180/80/160	0.16	-	-
45	90/60/30	0/90/150	0.84	90/60/30	0.16	160/60/140	0.17	-	-
46	90/60/60	319/41/130	0.88	110/60/40	0.19	140/40/120	0.21	-	-
47	90/60/90	270/30/90	0.77	70/40/100	0.15	0/40/90	0.17	-	-
48	90/90/0	0/0/90	0.67	90/80/10	0.19	180/80/170	0.21	-	-
49	90/90/30	300/90/120	0.61	90/80/20	0.16	1800/80/170	0.17	-	-
50	90/90/60	23/76/117	0.66	90/90/60	0.10	0/30/0	0.10	90/90/120	0.10

Table 5.5: Moment tensor ($\phi_s = 0^\circ, \delta = 90^\circ, \lambda = 90^\circ$).

$$\begin{vmatrix} 0.000 & 0.000 & 0.866 \\ 0.000 & 0.000 & -0.500 \\ 0.866 & -0.500 & 0.000 \end{vmatrix}$$

As pointed out earlier, not all of the multiple solutions, however, represent conjugate pairs. To understand these solutions, P waveforms at different azimuths are calculated using two different source mechanisms, $\phi_s = 30^\circ, \delta = 60^\circ, \lambda = 60^\circ$ and $\phi_s = 80^\circ, \delta = 50^\circ, \lambda = 130^\circ$ (Figure 5.21). At the distance ranges examined, the waveforms for these two different source mechanisms are identical. (Table 5.6) shows the moment tensors for each solution. The only significant difference between the two moment tensors are the $m_{1,3}$ and $m_{2,3}$ components.

Table 5.6: Moment tensor for two different source mechanisms ($\phi_s = 80^\circ, \delta = 50^\circ, \lambda = 130^\circ$ and $\phi_s = 30^\circ, \delta = 60^\circ, \lambda = 60^\circ$).

$$\begin{vmatrix} -0.563 & 0.592 & 0.203 \\ 0.592 & -0.191 & 0.384 \\ 0.203 & 0.384 & 0.754 \end{vmatrix} \quad \begin{vmatrix} -0.563 & 0.541 & 0.000 \\ 0.541 & -0.188 & -0.500 \\ 0.000 & -0.500 & 0.750 \end{vmatrix}$$

The coefficients of the fundamental Green's functions which are functions of moment tensor components calculated for these two different source mechanisms according to equation (2.10), C_1 for strike slip, C_2 for dip slip and C_3 for 45° dip slip

are shown in Table (5.7) for several azimuths. The coefficients of the strike slip and 45° dip slip contributions are very similar for both of the source mechanisms. The dip slip component, however, varies. The maximum amplitudes of the fundamental Green's functions are 4.0, 1.5, 0.5 for 45° dip slip, strike slip, and dip slip respectively. When we combine the fundamental Green's functions with these weighting coefficients, strike slip and 45° dip slip components will dominate, the contribution of dip slip component will be small. The small contribution of dip slip component, or $m_{1,3}$ and $m_{2,3}$ components of moment tensor, implies that ground motion is relatively insensitive to these components. The other important characteristic is similarity between strike slip component and 45° dip slip component. This also is the result of vanishing tangential component of moment tensor due to a shallow source and leading a linear dependence between weighting coefficients (equation 2.10). It is, therefore, impossible to resolve elements of two moment tensor components, $m_{1,3}$ and $m_{2,3}$, and distinguish between two source mechanisms for shallow sources (Dziewonski et al., 1981).

Table 5.8 compares the solutions shown in Tables 5.1-5.4. Error between the true solution and the solution found after the grid search which is the closest to the true solution is calculated and the ratio of maximum and minimum RMS errors for these solutions is constructed. Error in the source parameters and the ratio of the RMS errors will give an understanding of the effectiveness of the parameterizations.

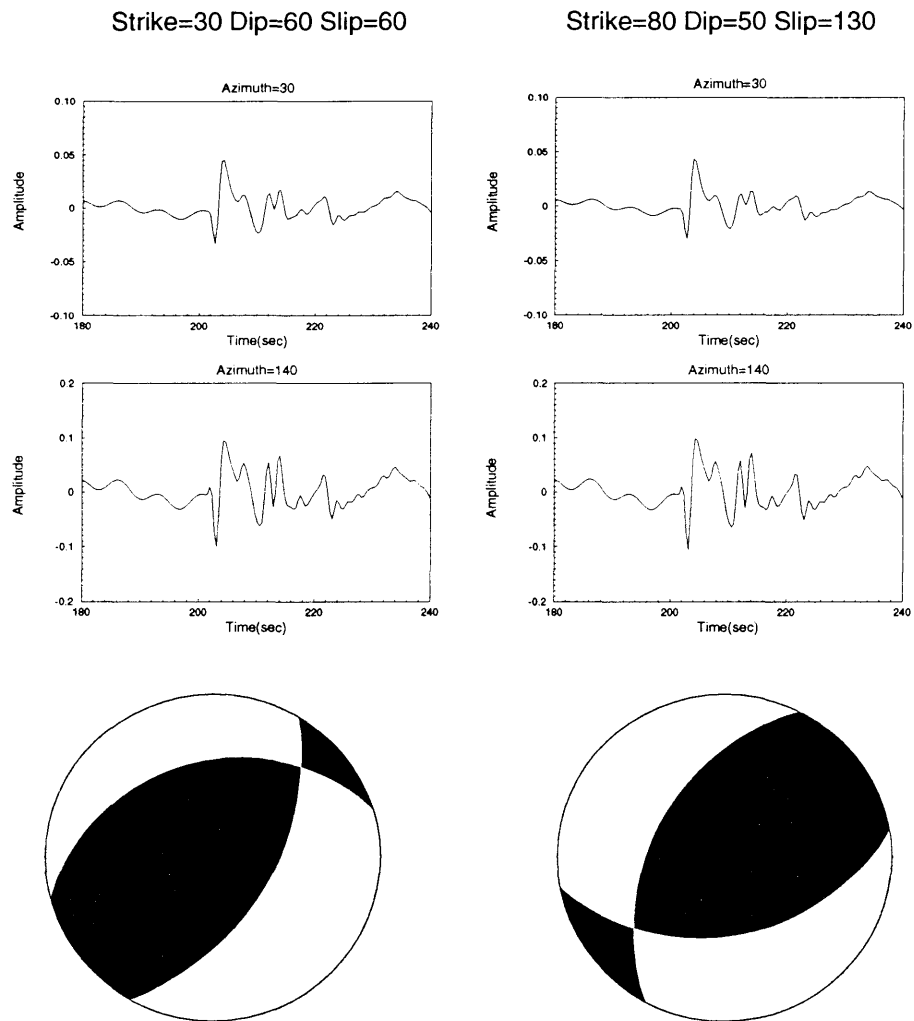


Figure 5.21: P waveforms generated at 2 different azimuths (top) are identical for two different source mechanisms (bottom) found after the grid search.

Table 5.7: Coefficients of fundamental Green's functions

$\phi_s = 80^\circ, \delta = 50^\circ, \lambda = 130^\circ$				$\phi_s = 30^\circ, \delta = 60^\circ, \lambda = 60^\circ$		
Azimuth	C_1	C_2	C_3	C_1	C_2	C_3
0	-0.563	0.203	0.754	-0.563	0.000	0.750
30	0.042	0.367	0.754	0.000	-0.250	0.750
60	0.228	0.434	0.754	0.187	-0.433	0.750
90	-0.191	0.384	0.754	-0.187	-0.500	0.750
200	-0.139	-0.322	0.754	-0.171	0.171	0.750

Table 5.8 also compares the error in the source parameters and the ratio of maximum and minimum RMS for different parameterizations and different time windows. The solutions found using the energy and the statistical moments of the *P-waves* are not considerably different since envelopes of the waveforms and absolute value of the waveforms are very similar. There are, however, large differences between the solutions found from the energy and statistical moments of the surface waves. The reason is that calculation of the envelope of a seismogram is an averaging process of the wavefield. This is, especially, true for surface waves since larger time windows are used for computation and envelopes pass over the peak values.

One of the important features to notice (Table 5.8) is that the ratio of RMS error decrease and the error between the true solution and estimated solution increase as the slip approaches to 90° . The best solutions are found when the source parameters, strike,dip,slip, are $\pm 20^\circ$ from the bounding values of the grid ($0^\circ, 90^\circ, 180^\circ$).

Table 5.8: A summary of Tables 5.1-5.4.

Trial	True Sol ³	P-waves						Surface waves					
		Energy			Moment			Energy			Moment		
		Error	$\frac{max}{min}$	RMS	Error	$\frac{max}{min}$	RMS	Error	$\frac{max}{min}$	RMS	Error	$\frac{max}{min}$	RMS
1	0/30/0	0/0/0		22.0	0/10/0	15.1	0/0/0	0/0/0	40.6	0/10/0	4.1		
2	0/30/30	0/0/0		12.5	0/10/0	10.9	10/10/20	27.6	0/0/30	6.1			
3	0/30/60	10/0/20		7.6	10/10/0	11.2	0/0/0	9.2	10/0/20	3.7			
4	0/30/90	10/10/20		7.8	10/10/0	13.9	10/0/20	9.7	10/20/10	3.6			
5	0/60/0	0/20/0		8.9	0/20/0	11.6	0/10/0	22.4	0/20/0	6.2			
6	0/60/30	0/10/30		7.8	0/0/0	7.6	0/10/10	23.1	0/10/10	4.1			
7	0/60/60	0/10/0		7.6	0/0/0	8.8	10/0/20	15.0	10/10/10	4.6			
8	0/60/90	0/20/0		8.4	0/10/0	13.3	10/30/20	9.6	10/10/10	5.3			
9	0/90/0	0/0/0		4.9	0/0/0	6.2	0/0/20	17.3	0/10/0	3.5			
10	30/30/30	0/0/0		15.3	0/0/0	12.3	0/0/0	28.9	0/0/0	6.1			
11	30/30/60	10/0/0		8.3	0/10/0	8.9	0/0/0	14.8	0/0/10	3.8			
12	30/30/90	0/0/20		6.9	10/20/10	11.1	10/0/20	11.9	10/10/10	4.1			
13	30/60/0	0/10/0		10.0	0/20/0	13.1	0/0/0	13.6	0/10/10	4.2			
14	30/60/30	0/0/0		9.3	0/0/0	8.1	0/10/10	24.6	0/10/10	4.8			
15	30/60/60	0/20/10		8.0	0/20/10	8.5	10/30/0	18.2	10/30/0	4.7			
16	30/60/90	10/20/20		6.8	10/20/10	10.3	10/30/20	11.7	0/20/20	4.1			
17	30/90/0	0/0/0		5.0	0/0/0	6.7	0/0/20	12.5	0/0/0	3.2			
18	30/90/30	0/0/20		10.0	0/0/20	13.1	0/0/0	14.5	0/10/20	4.1			
19	60/30/30	0/0/0		17.0	0/10/0	11.4	0/0/0	39.0	10/0/40	10.7			
20	60/30/60	0/0/0		9.2	0/10/0	8.8	0/0/0	15.4	10/0/0	5.0			
21	60/30/90	0/0/0		6.4	0/10/0	9.0	10/0/20	13.1	0/0/10	3.6			
22	60/60/90	0/0/0		6.4	0/10/0	9.3	0/0/0	13.6	0/0/0	3.6			
23	60/90/30	0/0/10		10.6	0/10/30	11.8	0/0/0	17.6	0/0/10	4.2			
24	60/90/60	0/0/0		28.6	0/0/10	14.3	0/0/0	67.3	0/0/0	7.8			
25	90/30/30	0/10/10		16.4	0/10/0	13.1	0/10/0	26.8	0/10/0	9.0			
26	90/60/60	10/10/0		10.1	0/10/10	7.3	10/10/20	17.7	20/10/20	4.6			
27	90/30/60	10/0/10		10.9	0/10/0	9.6	10/0/10	15.7	-	-			
28	90/60/90	10/10/10		6.9	0/10/0	9.3	10/0/10	15.9	20/20/10	5.1			
29	90/90/30	0/0/30		12.8	0/0/30	12.8	0/0/10	22.4	0/10/10	3.8			
30	90/90/60	0/0/10		14.6	0/0/10	14.6	0/0/0	39.4	0/0/0	6.6			

5.5 Inversion

A linear moment tensor inversion can be performed when a linear parametrization is used. This is valid only if amplitude or area is used as the parametrization. Since calculating the envelope of a seismogram is a nonlinear process with respect to the source parameters, strike, dip, and slip, the procedure outlined in Chapter 3 is used. Partial derivatives with respect to source parameters are calculated using the finite-difference method:

$$\hat{u}(t, p) = \frac{u(t, p + \Delta p) - u(t, p)}{\Delta p}, \quad (5.7)$$

with $\Delta p = 5^\circ$.

The inversion of the source parameters is performed as an alternative to the the grid search since the grid search requires too much computational time when sampling is smaller than 10° . The inversion converges after 10 – 20 iterations. As mentioned earlier, the success of the inversion depends on the initial estimate of the model parameters. Therefore, different initial models should be used. It is usually sufficient to start from 4 different corners of the grid. Since there are multiple solutions, each inversion may converge to different sets of source parameters.

The example used for the grid search, $\phi = 30, \delta = 60, \lambda = 60$, is used as a first example of the inversion. The two solutions found in the grid search are found using two different initial sets of parameters. The first solution is $\phi = 80, \delta = 40, \lambda = 132$ (Figure 5.22) and the second solution is $\phi = 30, \delta = 39, \lambda = 52$ (Figure 5.23).

The second example is chosen from Figure 5.18 for the source mechanism, $\phi = 0, \delta = 90, \lambda = 0$. Two different initial sets of parameters are used and two different solutions are found after inversion (Figure 5.24) and (Figure 5.25).

The solutions estimated from the inversions are shown in the the tables (5.1-5.4). There are, however, changes in the estimated source parameters and the level of the RMS error. The RMS errors found after the inversion are much smaller than those found using the grid search.

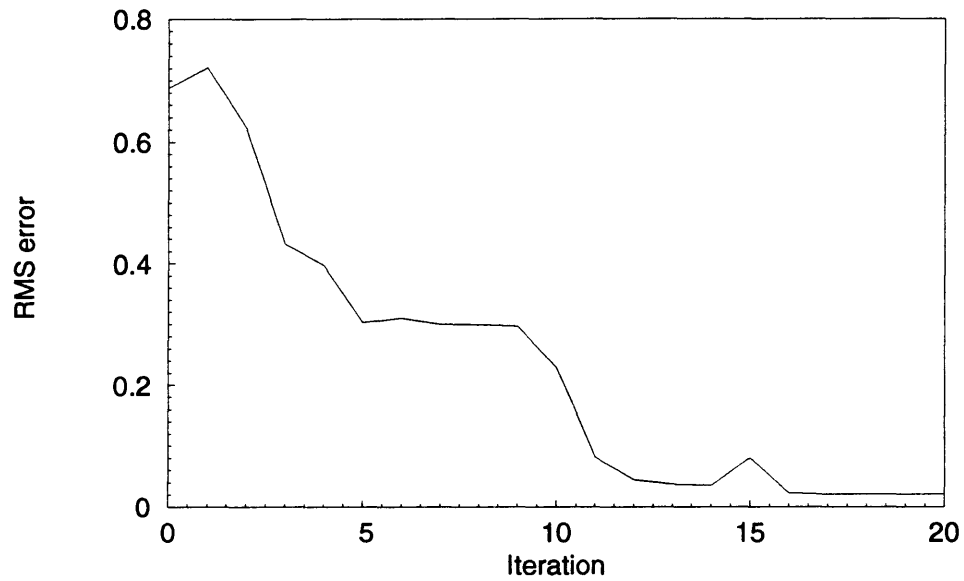


Figure 5.22: The change in the RMS error with iteration using moments of the *P-wave* envelopes.

Table 5.9: The estimated source parameters from an initial set of parameters.

Parameter	True Solution	Initial Model	Solution
Strike	30	180	80
Dip	60	0	41
Slip	60	180	132

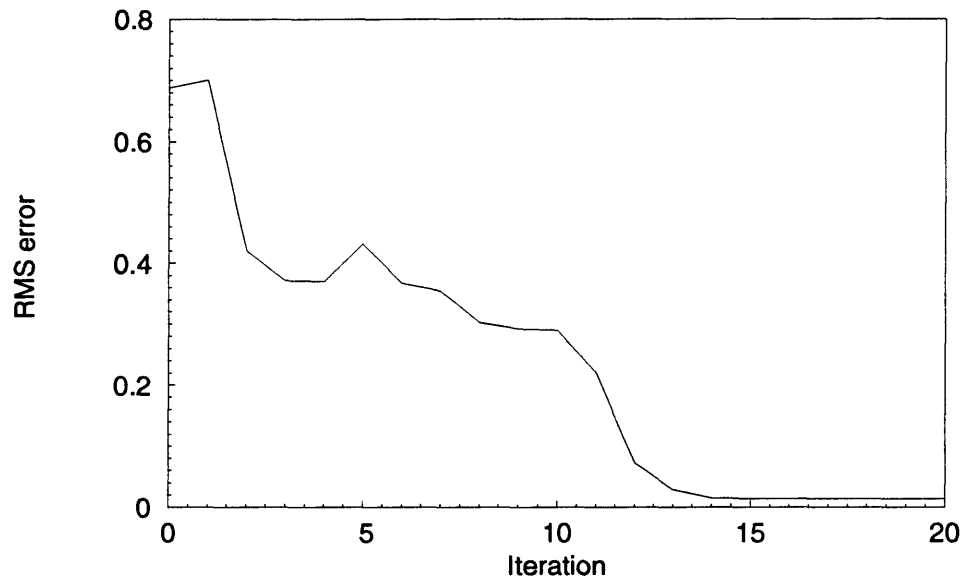


Figure 5.23: The change in the RMS error with iteration using moments of the *P-wave* envelopes.

Table 5.10: The estimated source parameters from an initial set of parameters.

Parameter	True Solution	Initial Model	Solution
Strike	30	10	30
Dip	60	10	39
Slip	60	10	52

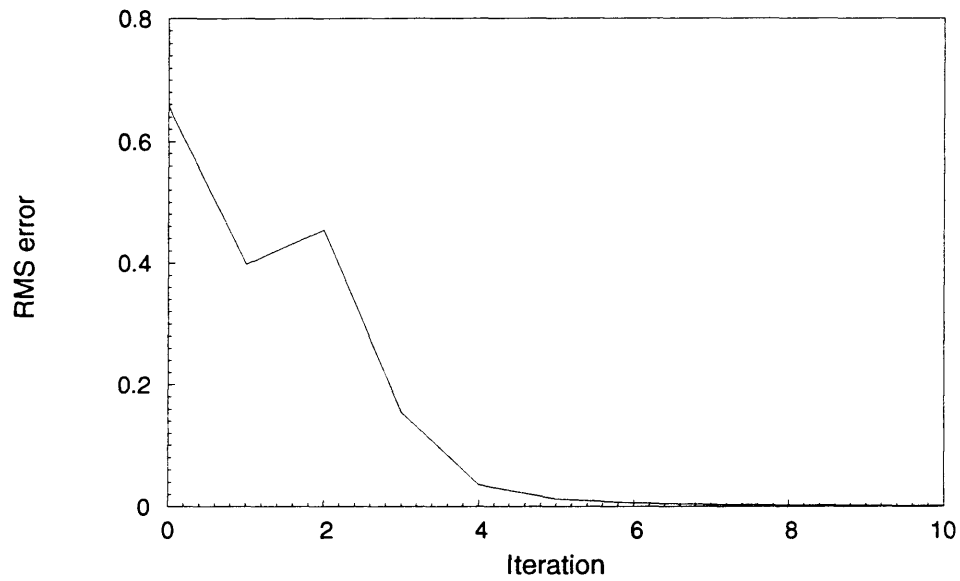


Figure 5.24: The change in the RMS error with iteration using moments of the surface wave envelopes.

Table 5.11: The estimated source parameters from an initial set of parameters.

Parameter	True Solution	Initial Model	Solution
Strike	0	90	90
Dip	90	90	90
Slip	0	90	178

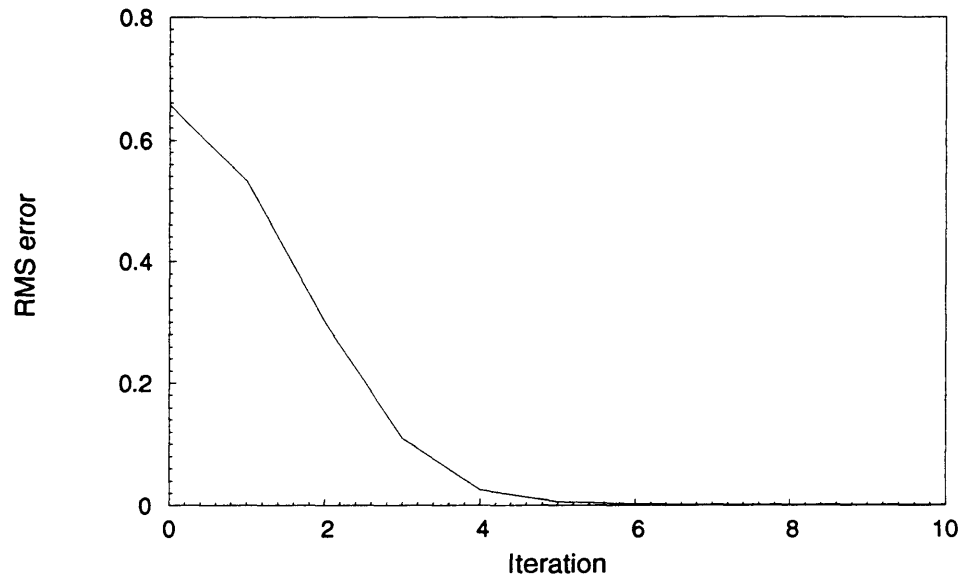


Figure 5.25: The change in the RMS error with iteration using moments of the surface wave envelopes.

Table 5.12: The estimated source parameters from an initial set of parameters.

Parameter	True Solution	Initial Model	Solution
Strike	0	0	0
Dip	90	0	88
Slip	0	0	0

Chapter 6

CONCLUSIONS

Observed waveforms at regional distances are affected by a crust which is very heterogeneous. Modeling the waveforms at these distances to recover earthquake source parameters requires the inclusion of a very complex laterally varying earth structure. Even if we could calculate synthetic seismograms in this structure, we could never hope to know the structure well enough. Since the difficulty is fundamental in modeling seismograms for three dimensional complex earth structures, it is important to develop parameterizations for source mechanism determination.

Computer simulations are performed to recover earthquake source parameters from regional waveforms. Lateral variations in earth structure are represented by randomly perturbing a reference earth model. Observed seismograms are calculated using the reference earth model and synthetic seismograms are calculated from the perturbed models. Parameterizations are developed using the seismograms and their envelopes. Parameterizations are tested for their sensitivity to different source mechanisms and structural variations. These parameterizations include area, energy of

the seismograms and higher order statistical moments of their envelopes.

Correlation coefficients are calculated between parametrizations of the observed seismograms and the calculated seismograms. It is found out that the energy of the seismograms and the statistical moments of the envelopes of the seismograms are sensitive to source mechanisms. A grid search is performed with a 10° spacing using these parameterizations over the source parameters and RMS errors between observed and calculated parameterizations are evaluated. Scalar seismic moment is estimated comparing zeroth moment of the envelope of the observed and the synthetic seismograms from the best solution found after the grid search.

A large number of experiments are performed using these parameterizations for different time windows, P-waves, surface waves. Parameterizations are successful in determining the source parameters. There are, however, multiple solutions for each experiment. Some of these solutions are recognized as conjugate fault solutions. The solutions which cannot be explained by conjugate fault plane are caused because of the small contribution of the dip slip component of the fundamental Green's functions. This the case when the source depth is smaller than the minimum wavelength in the data.

Errors between the true solution and the estimated solution are in the range of $\pm 30^\circ$. Solutions are well constrained when source parameters are $\pm 20^\circ$ away from the extreme values ($0^\circ, 90^\circ, 180^\circ$). The error is maximum and the ratio of the maximum

and minimum RMS is minimum when slip is close to 90° .

RMS error found from the energy and moments of P-waves is not significantly different. The solutions estimated using the energy of the surface waves have deeper minima than the moments of the envelopes of the surface waves. There are not, however, large differences in the estimated solutions.

The grid search is performed using tangential component of the wavefield as well. The tangential component at these distance range and for the specified earth model did not give satisfactory results.

Least-squares inversion is applied using these parametrizations as an alternative to the grid search. Source parameters are estimated after 10-20 iterations. It is recognized from the inversion that solutions found in the grid search have deeper minima. That is, a small search spacing may allow to determine the location of a global minimum with greater accuracy. The solutions found after inversion depend on the initial set of parameters.

Combining the tangential component of the wavefield may reduce the number of solutions although the results we obtained are not satisfactory. The solutions caused by the small contribution of dip slip component of the Green's functions can be eliminated by using a weight in the inversion for this term. The parametrizations should be tested further adding random noise to the synthetics. Synthetics should be calculated for more realistic earth models.

REFERENCES

- Aki, K., and Lee, W. H. K. 1976., Determination of three-dimensional velocity anomalies under a seismic array using first P arrival times from local earthquakes 1. A homogeneous model., Journal of Geophysical Research., 81: 4395-4402.
- Aki, K., and Richards G. P. 1980., Quantitative Seismology., San Fransisco: W. H. Freeman and Company.
- Bracewell, N. R. 1986. The Fourier Transform and Its Applications, New York: McGraw-Hill Book Company.
- Byerly, P. 1955. Nature of faulting as deduced from seismograms., Geol. Soc. Am. special paper, 62: 75-85.
- Chapman, C. H. 1978. A new method for computing synthetic seismograms., Geophys. J. R. Astr. Soc., 54: 481-513.
- Chapman, C. H., and Orcutt, J. A., 1985., The computation of body wave synthetic seismograms in laterally homogenous media., Rev. Geophys., 23: 105-163.
- Dziewonski, A. M., Chou, T. A and Woodhouse, J. H., 1981., Determination of Earthquake Source Parameters From Waveform Data for Studies of Global and Regional Seismicity., Geophys. Journal of Geophysical Research., 86: 2825-2852.
- Friyer, G. J. 1980., A slowness approach to the reflectivity method of seismogram synthesis., Geophys. J. R. Astr. Soc., 63: 747-758.
- Fucsh , K. and Muller, G. 1971., Computation of Synthetic Seismograms with the Reflectivity Method and comparision with the observations., Geophys. J. R. astr. Soc., 23: 417-433.

Gilbert, F., 1971., Excitation of the normal modes of the Earth by earthquake sources., Geophys. J. R. Astr. Soc., 22:223-226.

Gilbert, F. and Dziewonski, A. M. 1975., An application of normal mode theory to the retrieval of structural parameters and source mechanisms from seismic spectra., Phil. Trans. R. Soc., 278: 187-269.

Golub, G. H., and Reinsch, C. 1970., Singular Value Decomposition and Least-Squares Solutions., Handbook for Automatic Computation, II, Linear Algebra, Springer-Verlag, Berlin, Heidelberg, New York.

Helmberger, V. D., 1974., A procedure for modelling shallow dislocation sources., Geophys. J. R. astr. Soc., 42: 117-130.

Hodgson, J. H., 1953., Tables extending Byerly's fault-plane technique to earthquakes of any focal depth., Bull. Seismol. Soc. Am. Soc., 43: 49-61.

Honda, H., 1962., Earthquake Mechanism and seismic waves., Geophys. Notes, Faculty Sci., Tokyo University, 15: 1-97.

Keilis-Borok, V. I. 1959., An estimation of the displacement in an earthquake source and of source dimensions., Ann. Geofis., 12: 205-214.

Kennett, B. L. N., 1983., Seismic wave propagation in stratified media., Cambridge: Cambridge University Press.

Kind, R., 1985., Reflectivity Method: a tutorial., Journal of Geophysics., 58: 153-174.

Koch, R., 1991., Moment tensor inversion of local earthquake data-I. Investigation of the method and its numerical stability with model calculations., J. R. Astr. Soc., 58: 153-174.

Langston, A. C., and Helmberger, V. D., 1975., Generalized ray theory for shear dislocations., Bull. Seismol. Soc. Am., 64: 45-64.

Lees, J. M., and Malin, E. M., 1990., Tomographic Images of P-wave velocity variations at Parkfield, California., J. R. Astr. Soc., 95: 21793-21804.

Levenberg, K. 1944., A method for the solution of certain nonlinear problems in

- least squares., Quarterly of Applied Mathematics, 2: 164-168.
- Lines, R. L., and Treitel, S. 1988., Tutorial, A review of least-squares inversion and its application to geophysical problems., Geophysical Prospecting., 32: 159-186.
- Marquard, D. W. 1963., An algorithm for the least squares estimation of non-linear parameters, Journal of the Society of Industrial and Applied Mathematics, 11: 431-441.
- McCovan, D. W. 1976., Moment tensor representation of surface wave sources., Geophys. J. R. Astr. Soc., 44: 595-599.
- Nábělek's, J. L., 1984., Determination of earthquake source parameters from inversion of body waves., Ph.D. thesis, Mass. Inst. of Technol., Cambridge.
- Nakano, H. 1923., Notes on the nature of the forces which give rise to the earthquake motions., Seismol. Bull., Central Meteorological Obs., Japan, 1: 92-120.
- Nuttli, O., and Whitmore J. D. 1962., On the determination of polarization angle of the S wave., Bull. Seismol. Soc. Am., 52: 95-107.
- Saikia, K. J., and Herrmann, B. R. 1985., Application of waveform modeling to determine focal mechanisms of four Miramichi aftershocks., Bull. Seismol. Soc. Am., 75: 1021-1040.
- Saikia, K. J., and Herrmann, B. R. 1986., Moment-tensor solutions for three 1892 Arkansas swarm earthquakes by waveform modelling., Bull. Seismol. Soc. Am., 76: 709-723.
- Sipkin, A. S., 1982., Estimation of earthquake source parameters by the inversion of waveform data: Synthetic waveforms., Phys. Earth Planet. Inter., 30: 242-259.
- Stauder, W. 1962., The focal mechanism of earthquakes., Advances in Geophysics., New York: Academic., 9: 1-76.
- Strelitz, A. R., 1978., Moment tensor inversions and source models., Geophys. J. R. Astr. Soc., 52: 359-364.

Stump, B. W., 1976., The determination of source mechanisms by linear inversion of seismograms (abstract)., Trans. Am. Geophys. Un., 57: 953.

Stump, B. W., and Johnson, L. R., 1982., Higher-degree moment tensors-The importance of source finiteness and rupture propagation on seismograms., Geophys. J. R. Astr. Soc., 69: 721-743.

Wallace, A. S., 1978., Moment tensor inversions and source models., Geophys. J. R. Astr. Soc., 52: 359-364.

Appendix A

THE HILBERT TRANSFORM

The Hilbert Transform of $f(x)$ is defined as (Bracewell, 1986)

$$F_{Hi}(t) = \int_{-\infty}^{\infty} \frac{f(\acute{t})d\acute{t}}{\acute{t} - t}. \quad (\text{A.1})$$

The Cauchy principal value of the integral is calculated at $t = \acute{t}$. $F_{Hi}(t)$ can also be obtained from $f(t)$ by convolution with $(-\pi t)^{-1}$.

$$F_{Hi}(t) = \frac{-1}{\pi t} * f(t). \quad (\text{A.2})$$

The Fourier transform of $(-\pi t)^{-1}$ is $i \operatorname{sgn} f$ (Figure A.1), which is equal to $+i$ for positive f and $-i$ for negative f , hence the Hilbert transformation is equivalent to filtering $f(t)$, which the amplitudes of the spectral components are unchanged, but their phases are altered by $\frac{\pi}{2}$, positively and negatively according to the sign of f .

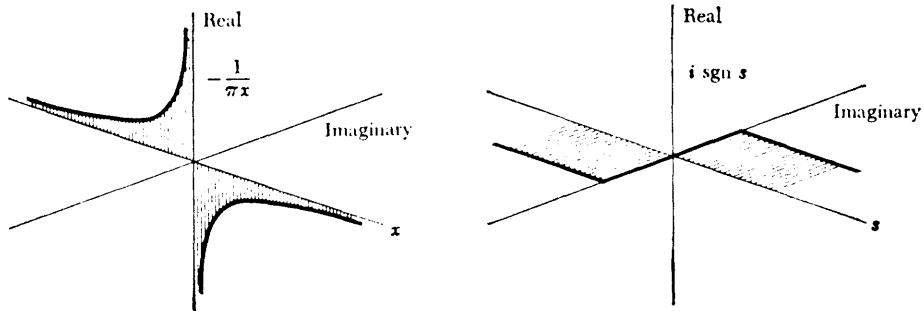


Figure A.1: The kernel $(-\pi t)^{\frac{1}{2}}$ and its Fourier transform $i \operatorname{sign} s$. Bracewell(1986).

The analytic signal is defined as

$$f_c(t) = f(t) - F_{Hi}(t). \quad (\text{A.3})$$

The analytic signal can be obtained from $f(t)$ by suppressing the negative frequencies. To show this, let $f(t) \supset F(f)$ and let $\hat{f}(t)$ be derived by suppressing negative frequencies and doubling:

$$\hat{f}(t) \supset 2H(f)F(f), \quad (\text{A.4})$$

since

$$H(f) \supset \frac{1}{2}\delta(f) + \frac{i}{2\pi f}, \quad (\text{A.5})$$

it follows that

$$\hat{f}(t) = 2\left(\frac{1}{2}\delta(f) + \frac{i}{2\pi f}\right) * f(t) \quad (\text{A.6})$$

$$= f(t) - i\left(\frac{-1}{\pi t}\right) * f(t), \quad (\text{A.7})$$

$$= f(t) - iF_{Hi}(t). \quad (\text{A.8})$$

The envelope, $E(t)$, of any function, $f(t)$, can be obtained by taking the modulus of equation A.8.

$$E(t) = (f(t)^2 + F_{Hi}(t)^2)^{\frac{1}{2}}. \quad (\text{A.9})$$